Lyman Break Galaxies at $z \sim 5$: Luminosity Function*

Ikuru Iwata,[1] Kouji Ohta,[1] Naoyuki Tamura,[1,2]
Masataka Ando,[1] Shinpei Wada,[1] Chisato Watanabe,[1]
Masayuki Akiyama,[3] and Kentaro Aoki[3,4]
[1]*Department of Astronomy, Faculty of Science, Kyoto University, Sakyo-ku, Kyoto 606-8502*
iwata@kusastro.kyoto-u.ac.jp
[2]*Department of Physics, University of Durham, Durham DH1 3LE UK*
[3]*Subaru Telescope, National Astronomical Observatory of Japan, 650 North A'ohoku Place, Hilo, Hawaii 96720 U.S.A*
[4]*Institute of Astronomy, The University of Tokyo, 2-21-1 Osawa, Mitaka, Tokyo 181-0015*

(Received 2002 August 25; accepted 2003 January 6)

Abstract

We present the results of a search for Lyman break galaxies (LBGs) at $z \sim 5$ in a 618 square-arcmin field including the Hubble Deep Field-North (HDF-N) taken by the Subaru Prime Focus Camera. Utilizing the published redshift data of the HDF-N and its flanking fields, the color selection criteria were chosen so that LBGs could be picked out most efficiently and least contaminated by foreground objects. The numbers of detected LBG candidates were 96 in $23.0 \leq I_c$ (mag) ≤ 24.5 and 310 in $23.0 \leq I_c \leq 25.5$. There is a hint of a deficiency of bright blue galaxies, although it is not as clear as has been suggested for LBGs at $z \sim 3$ to 4. With 305 LBG candidates in a 575 square-arcmin field, the rest-frame UV luminosity function of LBGs at $4.4 \lesssim z \lesssim 5.3$ was derived statistically by considering both the contamination by objects at the intermediate redshift and the incompleteness of the survey. The fraction of the contamination was estimated to be $\sim 50\%$ in the faintest magnitude range. The completeness of the survey was $\sim$80% at the bright part of the sample, and $\sim 20\%$ in the faintest magnitude range ($25.0 < I_c \leq 25.5$). The luminosity function of LBG candidates at $z \sim 5$ did not show a significant difference from those of LBGs at $z \sim 3$ and 4, though there might be a slight decrease in the fainter part. The UV luminosity density within the observational limit was 0.56—0.69 times smaller than that obtained for LBGs at $z \sim 3$, depending on the adopted cosmology and the integration range of the luminosity function. This decrease in the UV luminosity at $z \sim 5$ compared to that at $z \sim 3$ is due to the smaller number density of faint galaxies at $z \sim 5$. The similarity of the luminosity functions at redshifts 5 to 3 implies that

most of the LBGs at $z \sim 5$ should have faded out at $z \sim 3$, and that the LBGs at $z \sim 5$ are different galaxies from those seen at $z \sim 3$, if we take the face values for the ages of the LBGs at $z \sim 3$ obtained by a SED fitting in which a continuous star formation in an individual galaxy was assumed. However, if the star formation in LBGs is sporadic, the similarity of the luminosity function at $z \sim 3$ and 5 would be explained. Such sporadic star formation has been suggested by hydrodynamical simulations and semi-analytic models with collisional starbursts, and the trend of the cosmic star formation history predicted by these studies resembles that estimated from an integration of the UV luminosity density within the observational limit.

Key words: galaxies: evolution — galaxies: formation — galaxies: luminosity function – galaxies: Lyman break galaxies

1. Introduction

During the past several years, observational studies of galaxy formation and evolution have progressed remarkably. One of the most important progress is that the statistical nature of high-redshift galaxies has been revealed through the finding of many normal (non-AGN) galaxies at high redshift, which was enabled by the broad-band color selection method pioneered by Steidel and his collaborators (e.g., Steidel, Hamilton 1992; Steidel et al. 1996a). Since the method employs only broad-band imaging, it does not need a huge amount of telescope time, such as the optical spectroscopy of faint galaxies, and it efficiently finds galaxies at a targeted redshift. In fact, the redshifts of more than 80% of the galaxies selected by this method (called Lyman break galaxies) have been confirmed by optical spectroscopy (Steidel et al. 1996a, 1999).

Since their first discovery in the late 1990s, the Lyman break galaxies (LBGs) at $z \sim 3$ have been extensively investigated in various ways, and knowledge about their nature has been accumulated. Their rest UV spectra resemble those of nearby active star-forming galaxies (Steidel et al. 1996b). On-going star formation rates estimated from UV luminosities and from emission lines in rest-frame optical band are up to several tens of $M_\odot$ yr^{-1} (e.g., Steidel et al. 1996b; Pettini et al. 2001). Their stellar population was investigated by comparing the optical to near-infrared spectral energy distributions (SEDs) with stellar population synthesis models (Sawicki, Yee 1998; Papovich et al. 2001; Shapley et al. 2001). It is found that most of the LBGs at $z \sim 3$ are well fitted by models dominated by a young stellar population with ages ranging from 10 Myr to 1 Gyr with moderate dust extinction [$E(B-V) \sim 0.1$–0.4]; their typical stellar mass was estimated to be $\sim 10^{10}$ $M_\odot$, similar to a typical bulge mass of a present-day giant galaxy. The metal abundance in ionized gas was estimated through the rest optical emission

* Based on data collected at Subaru Telescope, which is operated by the National Astronomical Observatory of Japan.

line ratios to be sub-solar, similar to those of Large and Small Magellanic Clouds (Teplitz et al. 2000; Pettini et al. 2001). A clear signal of spatial clustering of the LBGs at $z \sim 3$ has been reported (Steidel et al. 1998; Giavalisco et al. 1998), and a comparison with models of cold dark matter (CDM) halos suggests that their clustering properties of the LBGs can be ascribed to biased galaxy formation (Giavalisco, Dickinson 2001).

Steidel et al. (1999) extend their ground-based LBG search to $z \sim 4$. They surveyed a 828 arcmin^2 area in total, which included 10 fields and found 244 galaxies with $I_{\rm AB} \leq 25.0$ mag. The luminosity function of the LBGs at $z \sim 4$ remarkably resembles that at $z \sim 3$, indicating that no significant evolution of the luminosity function occurs from $z = 4$ to $z = 3$ (about 0.6 Gyr for the cosmology with $\Omega_{\rm M} = 0.3$, $\Omega_\Lambda = 0.7$, and $H_0 = 65$ km s^{-1} Mpc^{-1}). Ouchi et al. (2001a) have also reported on the results of their own LBG survey for $z \sim 4$ in the field of SUBARU/XMM Deep Survey. They found that the luminosity function almost agrees with that obtained by Steidel et al. (1999), and that significant clustering was also seen.

The LBGs make a statistical sample of UV luminous objects at high redshift. Since the UV luminosity density is considered to be correlated with star-formation rate per unit volume, the LBGs have opened up the possibility to examine the star-formation history in the early universe (Madau et al. 1996, 1998). Steidel et al. (1999) found that the UV luminosity density at $z \sim 4$ is almost comparable to that at $z \sim 3$. If a correction for the dust extinction is applied, the star-formation densities at $z = 3$ and 4 are comparable to the value at z=1–2. The similarity in the luminosity function of LBGs at $z = 3$ and at $z = 4$ and the rather flat (extinction corrected) star-formation density history in $1 < z < 4$ are quite interesting, and may be a key property to understand the star-formation history of galaxies. As mentioned above, the ages of the LBGs at $z = 3$ are estimated to be 10 Myr to 1 Gyr with a median value of 0.1–0.3 Gyr based on SED fitting analyses by assuming continuous star formation. If these ages can be regarded as time intervals from the onset of the first star formation, the LBGs at $z \sim 3$ should be very young and most of them should form at $z < 4$ (e.g., Papovich et al. 2001). Accordingly, the star-formation density contributed by the LBGs at $z \sim 3$ should be lower by a factor of about 10 at $z > 4$ (Ferguson et al. 2002) and the LBGs at $z \sim 3$ must be different from the LBGs at $z \gtrsim 4$.

By using semi-analytic models based on a hierarchical clustering scenario, several authors tested whether the observed number densities and star-formation densities at $z \sim 3$ and $z \sim 4$ can be reproduced (e.g., Baugh et al. 1998; Somerville et al. 2001; Balland et al. 2002). Somerville et al. (2001) examine the nature of these LBGs using semi-analytic models, including starburst induced by the collision of galaxies as well as continuous star formation. They claim that their model with collisional starburst reproduces the observed luminosity functions of LBGs both at $z = 3$ and $z = 4$ with a reasonable amount of dust extinction, and the estimated star-formation density is claimed to be compatible with observations. On the other hand, the model with constant star formation efficiency (which does not include collisional starburst) fails to

reproduce the observed luminosity function of LBGs at $z \sim 3$, and the star-formation density declines rapidly at $z > 2$.

Pushing these studies back to the earlier universe and disclosing the nature of higher redshift galaxies is an obvious next target. The extension of the observational data toward higher redshift provides a stronger constraint on the physical processes of galaxy evolution through a comparison with theoretical models. It is also indispensable to study the epoch of the generation of the first galaxies. A study at higher redshifts has further importance, because it is approaching the suggested epoch of the cosmological reionization ($z \gtrsim 6$; Becker et al. 2001). The number densities of the LBGs may provide a constraint on determining the contribution of the star-forming galaxies to the ionizing background radiation (Madau et al. 1999). The discoveries of several star-forming galaxies at $z \gtrsim 5$ have already been reported (e.g., Dey et al. 1998; Weymann et al. 1998; Spinrad et al. 1998; Dawson et al. 2001; Ellis et al. 2001; Dawson et al. 2002). Their properties are important in the context of investigating the nature of galaxies at a high redshift. However, since there has not been a volume-limited large sample, the statistical properties of galaxies at $z \sim 5$ remain unknown. Finding many galaxies at $z \sim 5$ systematically and studying their statistical nature is necessary for the first step. We should carry out a survey with a sufficiently large search area at a deep limiting magnitude. However, it is not easy regarding technical aspects. The distances to the objects are becoming larger, and thus the apparent magnitude and surface brightness are becoming fainter. Consequently, the number density at an apparent magnitude decreases rapidly. In addition, the observing band shifts to a redder wavelength region where the OH sky emission increases the background noise. Therefore, a large aperture of the telescope and a wide field of view are required to perform this task.

Here, we present the first results of our survey of LBGs at $z \sim 5$ using the Subaru Prime Focus Camera (Suprime-Cam; Miyazaki et al. 2002), utilizing its unique capability of a wide field of view among 8 m class telescopes. We chose a sky area including the Hubble Deep Field-North (HDF-N; Williams et al. 1996), because there is plenty of information about galaxies with a wide redshift range ($0 < z < 6$). This database is quite powerful to examine our method for searching for galaxies at $z \sim 5$ and to obtain a reliable sample of candidates, under the circumstances that considerably time consuming optical follow-up spectroscopy must be carried out after making a candidate catalog. The field is also a sky area where many deep surveys at a variety of wavelengths, such as X-ray, infrared and radio, have accumulated. We will be able to utilize these data to investigate nature of the LBG population in other wavebands.

This paper is organized as follows. In section 2, the observations and procedures of data reduction are described. In section 3, criteria for finding LBGs at $z \sim 5$ and the number of objects detected are presented. The properties of the LBG candidates are also described. Then, in section 4, we quantify the corrections needed to apply to the observed data for deriving the luminosity function statistically, and the resultant luminosity function of LBGs at $z \sim 5$

is presented. In section 5, the implications of our findings to the evolution process of LBGs and the evolution of the UV luminosity density over the cosmic time scale are discussed. The contribution of LBGs at $z \sim 5$ to the UV ionizing field is also mentioned. In section 6 we give a summary and conclusion of our findings.

We use a set of cosmological parameters ($H_0 = 65$ km s^{-1} Mpc^{-1}, $\Omega_{\rm M} = 0.3$, and $\Omega_\Lambda = 0.7$) as the primary set, and in some cases we also use an Einstein–de Sitter universe model with $H_0 = 50$ km s^{-1} Mpc^{-1}, $\Omega_{\rm M} = 1.0$, and $\Omega_\Lambda = 0$, which had been commonly used as a standard set of cosmological parameters. The magnitude system is based on the Vega magnitude, except for those cases noted otherwise.

2. Observation and Data Reduction

2.1. Filter Selection

Prior to the observation, a combination of filters suited to isolate the $z \sim 5$ population was explored using mock galaxy spectra constructed with stellar population synthesis codes. Although it is not obvious that SEDs of LBGs at $z \sim 5$ are similar to those at $z \sim 3$, we adopted model SEDs of LBGs at $z \sim 5$ to enclose various rest-frame UV SEDs of LBGs at $z \sim 3$. The model spectrum for young, actively star-forming galaxies, by which we intend to model the SED of LBGs with the bluest UV color, was constructed using a stellar synthesis code developed by Kodama and Arimoto (1997). We included attenuation due to the inter-galactic medium, following a prescription by Madau (1995). In order to have the model spectra delineate the redder SED of LBGs, we adopted to take into account a reddening effect by dust within the object itself using an extinction curve given by Calzetti et al. (2000) with $E(B-V)$ from 0.0 to 0.4. In figure 1 we show the SEDs of the model spectra with $E(B-V) = 0.0$, 0.2 and 0.4, as well as the rest-frame photometric data points of LBGs at $z \sim 3$ in the HDF-N (Papovich et al. 2001). The model spectra reasonably cover the UV colors of the LBGs at $z \sim 3$. The adoption of the dust extinction is rather arbitrary to reproduce the redder colors of LBGs. The interpretation is, however, often used to derive color excesses in LBGs (e.g., Steidel et al. 1999).

We also prepared model spectra of spiral and elliptical galaxies for examining the efficiency of eliminating galaxies at intermediate redshifts. As spectra of spiral galaxies we used those of Sbc and Scd galaxies derived by Coleman et al. (1980). As a spectrum of an elliptical galaxy we employed a model spectrum by Kodama and Arimoto (1997), which reproduces the color–magnitude relation of elliptical galaxies observed in the local universe. We then calculated observed spectra for each type of galaxy from $z = 0$ to $z = 6$ with a step of 0.1. We did not consider any effect of evolution for all types of galaxies.

A desirable combination of filters should give the most distinct separation of the $z \sim 5$ population apart from the objects with smaller redshifts. We chose a combination of V, I_c, and z'-bands. In figure 2a, we show a two-color $V - I_c$ versus $I_c - z'$ diagram. It can be seen that

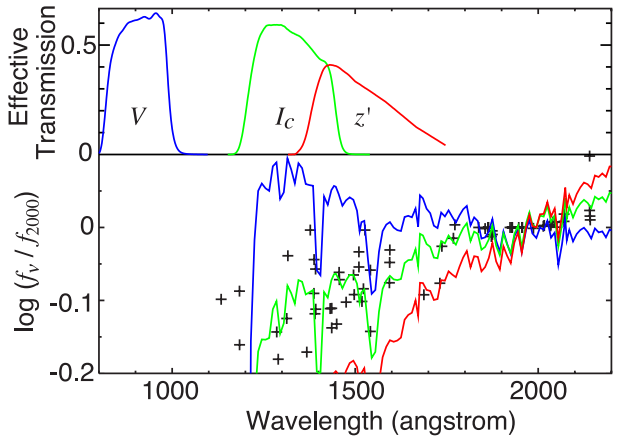

Fig. 1. Model UV spectra of LBGs at $z \sim 5$, which were used for the filter selection and to evaluate the incompleteness of our survey via a Monte Carlo simulation (in subsection 5.2). The bluest (extinction-free) spectrum is shown in the blue solid line. The green and red lines are spectra of the redder LBGs attenuated by dust with $E(B-V) = 0.2$ and 0.4, respectively. The attenuation by the intergalactic matter is taken into account (Madau 1995). The points are photometric data of the LBGs in the HDF-N at $z \sim 3$ (Papovich et al. 2001); we intend to cover the various SEDs at $z \sim 3$ by model spectra. All of the flux densities are normalized at 2000 Å. In the upper side of the figure we show the effective band-passes of the Suprime-Cam with V, I_c, and z' filters, which are blueshifted as they work for an object at $z = 5$.

galaxies at $z > 4.5$ can be well separated from foreground objects in the diagram. The most critical contamination is caused by elliptical galaxies at $z \sim 0.5$ due to the 4000 Å break and early-type spirals at intermediate redshifts.

Selecting the R-band instead of the V-band may also be reasonable, because of the high quantum efficiency at the band. However, contamination by galaxies with the 4000 Å break at intermediate redshifts is more serious than the adopted filter combination. Another reason that we did not choose the R-band is that the continuum depletion from the Lyman alpha forest should be heavier in the V-band, and a clear Lyman break makes it easier to isolate LBGs in a two-color diagram.

2.2. Observations

The observations were carried out on 2001 February 22 and 23 with Suprime-Cam attached to Subaru telescope at Mauna Kea. The Suprime-Cam consists of 10 mosaiced CCDs, each of which has a dimension of 2046 by 4090 pixels with a pixel scale of 0.″2. Each CCD covers a field of $\sim 7'$ by $\sim 13'$, and the typical gap between the CCDs is 10″–15″. The details of the observation are summarized in table 1. Note that our observations were made before the upgrade of the CCD array configuration held in 2001 April, and one CCD chip (at the north-west corner) was not working and another chip (at the south-west corner) had many bad columns. Thus, 8 CCDs were effectively working, and an $\sim 27'$ by $\sim 27'$ field is covered by a exposure.

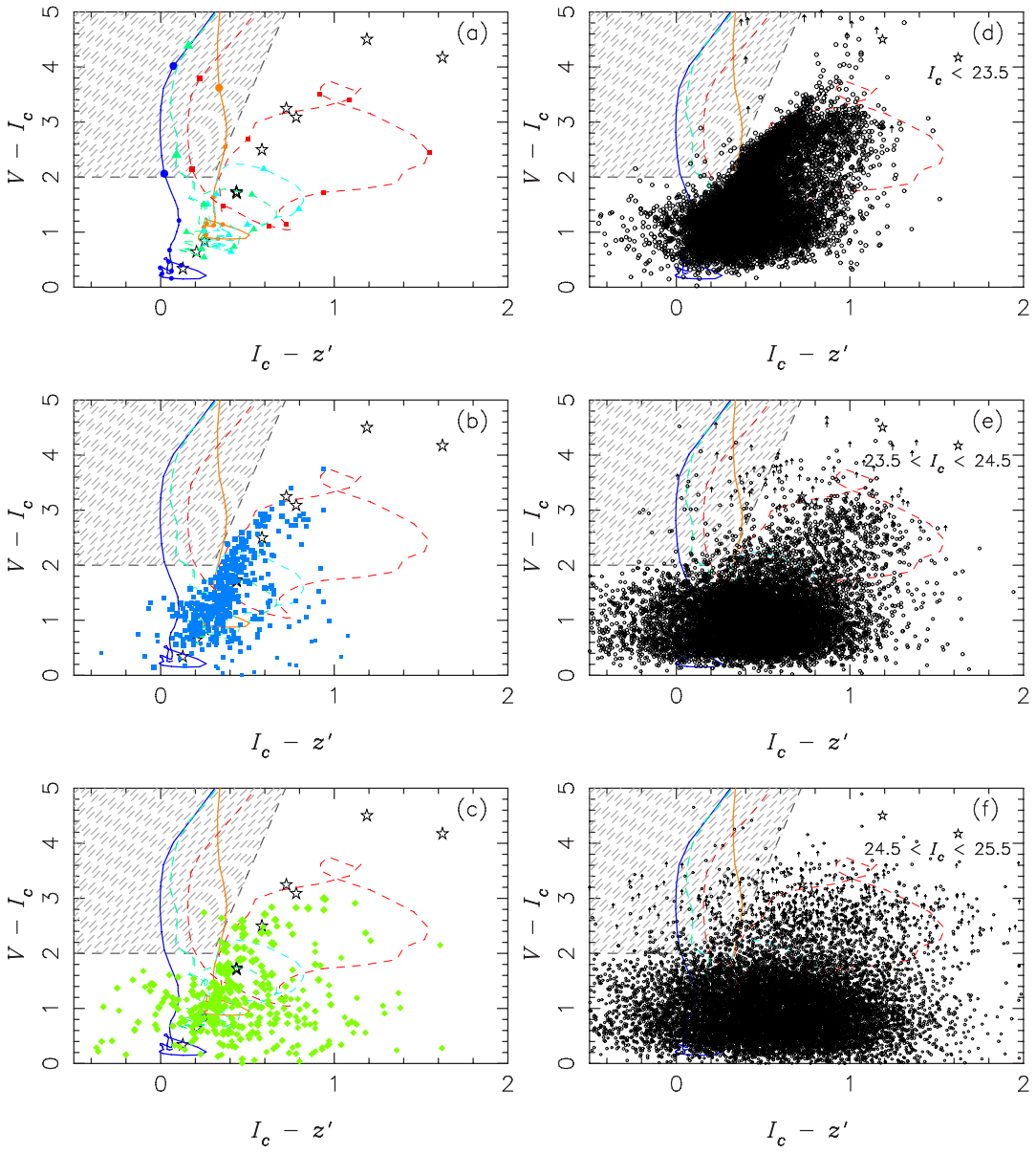

Fig. 2. $I_c - z'$ versus $V - I_c$ diagrams. **(a):** Tracks of colors for model galaxies at redshifts ranging from 0 to 5.5. A blue [an orange] line represents a galaxy with the bluest [reddest] model spectrum, i.e., $E(B-V) = 0.0$ [$E(B-V) = 0.4$] (see figure 1). A green and cyan dashed lines refer to local spiral galaxies (green is for Sbc, and cyan is for Scd; Coleman et al. 1980). A red dashed line is for a local elliptical galaxy. No evolution is considered. The symbols are plotted at a redshift interval of 0.5, and the symbols at $z \geq 4.5$ are enlarged. Star-symbols indicate the colors of A0–M9 stars calculated based on the library by Pickles (1998). The hatched region indicates the color criteria which we adopted for $z \sim 5$ galaxies. **(b):** Colors of galaxies cataloged in the spectroscopic survey of galaxies in the HDF-N and its flanking fields by Cohen et al. (2000) and identified in our image. All galaxies with the redshift range $z < 4.5$ are plotted. Tracks for model spectra are also shown. **(c):** Same as (b), but for galaxies in the HDF-N for which the photometric redshifts are given by Fernández-Soto et al. (1999) as $z < 4.5$. **(d) – (f):** The color distribution of the sources extracted from our image. Panels (d), (e) and (f) show objects with $I_c \leq 23.5$, $23.5 < I_c \leq 24.5$, and $24.5 < I_c \leq 25.5$, respectively. The circles are objects detected in all of the V, I_c, and z'-bands, and the arrows are those detected in I_c and z', but not in the V-band. The lower limits of $V - I_c$ colors are given for them.

Table 1. Details of the observation.

Dates	2001 February 22 and 23		
CCD dimension	9 CCDs with 2046 × 4090 pixels		
Pixel scale	$0.2''$/pixel		
Field of view / Effective surveyed area*	836 arcmin^2 / 575 arcmin^2		
Filters	V	I_c	z'
Effective integration time	21,600 s	2,520 s	3,100 s
Seeing	$0''.8$–$1''.0$	$0''.7$–$1''.0$	$0''.6$–$1''.0$
Magnitude of 5σ detection limit†	28.5 mag	25.5 mag	25.2 mag

* The effective surveyed area represents the area used to derive the luminosity function.

† The magnitude of the faintest object that can achieve S/N of 5 with the typical aperture size corresponding to the area of the detected sources at the magnitude range ($0''.9$ for V and z'-bands, $1''.2$ for I_c-band).

The imaging observation was made toward the Hubble Deep Field-North [RA(2000) = $12^{\rm h}36^{\rm m}49^{\rm s}.4$, Dec(2000) = $+62^\circ12'58''$]. Images were taken with a small dithering (typically $20''$) and a typical exposure time of 1440 s, 180–240 s, and 120 s, for V, I_c, and z'-bands, respectively for each exposure. The seeing size during the observations was typically $\sim 0''.9$; we discarded some frames with a median FWHM of stars larger than $1''.0$ for keeping the angular resolutions of the final images. The effective integration times were 21.6 ks, 2.5ks, and 3.1 ks for the V, I_c, and z'-bands, respectively.

2.3. Data Reduction and Calibration

The data reduction was carried out in a standard manner using IRAF[1] for basic data processing; the bias was subtracted using counts in an overscan region, and flat field frames were made by using normalized average of the object frames. The sensitivity differences between the CCD chips were corrected using the relative count rates of the flat-fielded dome flat frames for all three bands. The background was subtracted by a two-dimensional polynomial fitting. The positions of the frames were aligned by measuring the positions of the field stars which appeared commonly in all frames, and fitting fourth-order polynomial functions for coordinate conversion. The counts of each frame were adjusted by comparing the count-rate of the field stars common to all frames for every filter; after we measured the counts of field stars in each frame, the images were divided by the median of the count ratios of stars relative to a fiducial frame, so that the counts of stars are almost constant among the frames.[2] The images were

[1] IRAF is distributed by the National Optical Astronomy Observatories, which are operated by the Association of Universities for Research in Astronomy, Inc., under cooperative agreement with the National Science Foundation, USA.

[2] In this procedure, we found that although the variance of the flux ratios is stable and is well correlated with the airmass of the observed sky region on February 23, the flux ratio varies largely and the correlation of

convolved so that the median FWHM of the stellar sources matched within 10% for all frames in three bands.

Photometric calibrations for V and I_c-band images were made using images of photometric standard stars in Landolt (1992). The accuracy was ~ 0.02 mag for V and ~ 0.08 mag for I_c. For a photometric calibration of the z-band images, we employed two ways, both based on the $I_c - z'$ color. We first set an arbitrary zero point for the z' magnitude. In the first method, we examined the distribution of the $V - I_c$ and $I_c - z'$ colors of field stars exposed on our images. Next, we calculated the $I_c - z'$ colors to be observed with the system sensitivity of Suprime-Cam for the stars in the stellar flux library by Pickles (1998). We can determine the magnitude zero point for the z'-band by comparing the distribution of these colors. Another method is to use the spectral energy distribution of the galaxies in the HDF-N and its flanking fields. We used the galaxies for which the published V, I and J-band magnitudes are available, and estimated their $I_c - z'$ colors by linear interpolation. A comparison with the colors in our image gave the magnitude zero point. We adopted the magnitude zero point determined by the latter method. The z' magnitude zero points derived by these two methods agrees within ~ 0.1 mag in the color range of $I_c - z'$ between ~ 0 and 1. The z'-band magnitude is also based on Vega. We used the flux density table of Vega given by Castelli and Kurucz (1994), and applied $z'(\mathrm{AB}) - z'(\mathrm{Vega}) = 0.5505$.

2.4. Source Detection

Prior to extraction of astronomical objects from the final imaging data, we set masks for source detection around the bright objects in order to avoid any misidentification of the noise or tails of the bright objects as an individual object. We also removed the edge regions of each CCD chip from the object detection because of their low signal-to-noise ratio caused by dithering imaging. In total 26.1% of the CCD chip area is masked, and the effective area observed is 618.6 arcmin^2 (575.0 arcmin^2 without the CCD chip with many bad columns).

We used the software SExtractor (Bertin, Arnouts 1996) for the source detection and photometry. The primary parameters for the object detection are the threshold of counts above which the pixel is treated as a part of an object and the minimum number of connected pixels to be classified as an object. We extensively examined these parameters by comparing the detected sources with the objects in the HDF catalog version 2 (Williams et al. 1996) brighter than $I_{\mathrm{AB}}(814) = 27$, to minimize both the rate of noise contamination and the rate of missing objects. We also tested some spatial smoothing filters and adopted a Gaussian smoothing filter with a FWHM of 3 pixels for the I_c and z'-bands.

---

the flux ratio and the airmass is weaker on February 22. This suggests that the sky condition of the second observing night was better than the first night. Thus we selected one frame per filter as a fiducial frame, which was taken on the second night and the observed time is close to that of the exposures for standard stars. We adjusted the count-rate of the frames taken on the first night and other frames taken on the second night according to the fiducial frame.

The best set of parameters with which the detection rate of faint objects and the noise contamination are compromised is that the thresholds are 1.3, 1.0, 1.0 times the pixel-based background noise for V, I_c, and z', respectively, and to have at least 4 connected pixels above the threshold in each band. We regardeded sources in different bands as the same object whose pixel coordinates are within $1.0''$. We picked out objects only if they are detected both in I_c and z'-bands. The number of thus-selected sources was 29,094 for $I_c \leq 25.0$ and 35,362 for $I_c \leq 25.5$ in the 9 CCD chips. Although the adopted detection criteria seem to be loose, i.e., seem to tend to pick out many noise features, the criterion of two-band detection removes any spurious sources efficiently. It would be clarified by a comparison of the detected objects to the HST/WFPC2 data of HDF-N (Williams et al. 1996), which have deeper $V(606)$ and $I(814)$ images. There is no misidentification of noise as an object in $I_c \leq 24.5$, and the number of noise misidentification in $24.5 < I_c \leq 25.0$ is two among 55 extracted sources within the HDF-N region. Even in the magnitude range $25.0 < I_c \leq 25.5$, which is the faintest range we used, the rate of misidentification of noise was not very large; it was $\sim 17\%$. Many of these spurious sources are located close to objects which are relatively bright (but fainter than masked objects). These objects degrade the quality of flat field around them, and presumably cause misidentification. The number of selected sources are robust for changes of the detection parameters; if we adopt 10 pixels for the minimum connection of pixels for the V and I_c-bands, we only lose $\sim 2\%$ of the objects at the faintest magnitude range. The vast majority of selected objects have an area larger than 10 pixels in the I_c-band. The fraction of selected objects in our image among the HDF-N catalog is becoming smaller as the magnitude becomes fainter: ~ 100 % for $I_{\rm AB}(814) \leq 25$, ~ 67 % for $25 < I_{\rm AB}(814) \leq 25.5$, ~ 28 % for $25.5 < I_{\rm AB}(814) \leq 26.0$. The detection rates in other CCD chips do not change much, as described in subsection 4.1. The number counts in the I_c-band give 4.0×10^4 deg^{-2} mag^{-1} for $23.0 < I_c \leq 23.5$, 5.6×10^4 for $23.5 < I_c \leq 24.0$, 7.4×10^4 for $24.0 < I_c \leq 24.5$, 8.3×10^4 for $24.5 < I_c \leq 25.0$, and 7.7×10^4 for $25.0 < I_c \leq 25.5$. If we correct the incompleteness of our source detection, the number counts of our data agree well with those which appeared in previous studies (e.g., Tyson 1988; Williams et al. 1996).

Photometry of the detected objects was also made using SExtractor. We used the value "best magnitude" in SExtractor for the I_c magnitude and a $1.''6$ diameter aperture magnitude for the $V - I_c$ and $I_c - z'$ colors. The photometric accuracies were estimated by putting many artificial objects into our final images, executing detection and photometry with the same manner for the observed data and comparing the returned value with the original magnitude. The sizes and apparent magnitudes of the artificial objects were adjusted so that the obtained magnitude and size distribution would be similar to that of the real data. The r.m.s. errors of the I_c-band "best magnitude" for objects with $24.0 < I_c \leq 24.5$, $24.5 < I_c \leq 25.0$, and $25.0 < I_c \leq 25.5$ were 0.28, 0.35, and 0.41 mag, respectively. These error values are roughly consistent with the errors of I_c magnitude estimated from a comparison with the I_{814} magnitude for those objects in the HDF-N region. The photometric errors for V-band data were 0.22, 0.31, and 0.33

mag for $26 < V \leq 26.5$, $26.5 < V \leq 27.0$, and $27.0 < V \leq 27.5$, respectively, and for z'-band data, 0.39 mag, 0.45 mag, and 0.49 mag for $23.5 < z' \leq 24.0$, $24.0 < z' \leq 24.5$, and $24.5 < z' \leq 25.5$, respectively. The errors in $V - I_c$ and $I_c - z'$ colors, which were measured with a $1\farcs6$ aperture magnitude, were smaller than the errors in the total magnitude. The r.m.s. errors of background noise in the I_c-band, which were measured at randomly selected positions in our image with a $1\farcs6$ aperture, were 0.08 mag and 0.28 mag for $I_c = 24.0$ and 25.5, respectively. For the V-band data, they were 0.07 mag and 0.25 mag for $V = 26.0$ and 27.5, respectively; for the z'-band data, they were 0.18 mag and 0.40 mag for $z' = 24.0$ and 25.0, respectively.

The astrometry for the detected objects was made using stars in our field-of-view listed in the APM sky catalog (Irwin et al. 1994). We added stars from USNO-A2.0 (Monet et al. 1998) to increase the number of stars to calculate the conversion coefficients. There is no systematic error larger than $0\farcs3$ between these two catalogues in our region. We measured the positions of the stars in our I_c-band final image, and fitted a fourth-order polynomial function to minimize the χ^2 of the positional errors, for conversion of the positions in our images to equatorial coordinates. The relative positions of CCD chips were also adjusted to provide a minimum error for the coordinate conversion. The achieved internal positional accuracy was $\sim 0\farcs4$ r.m.s. for most parts of the image, and $\sim 1''$ at one CCD chip with many bad columns at the south-west corner.

3. Lyman Break Galaxy Candidates at $z \sim 5$

3.1. Selection Criteria

One of the most serious problems in a study of the statistical properties of Lyman break galaxies is a certain amount of contamination by objects located between us and the objects at the targeted redshift (so called 'interlopers'). The uncertainty of the fraction of the contamination affects the reliability of the statistical properties of the population, such as the luminosity function or the amplitude of the clustering. In figure 2a, we can see that a galaxy with an old stellar population (red dashed line) at $z \sim 0.5$ is close to the selection window for $z \sim 5$ galaxies; the 4000 Å break in a galaxy at $z \sim 0.5$ mimics the color by the Lyman break at $z \sim 5$.

In order to determine the selection criteria for galaxies at $z \sim 5$ as reliably as possible, we utilized previously published redshift data of the HDF-N and its flanking fields. We used a list of galaxies in the HDF-N and the flanking fields by Caltech Faint Galaxy Redshift Survey (CFGRS; Cohen et al. 2000) and the catalog of photometric redshift of galaxies in the HDF-N by Fernández-Soto et al. (1999). The magnitude limit is $R \sim 25.5$ mag for the CFGRS catalog and $I_{\rm AB}(814) = 28.0$ mag for the photometric redshift catalog. In our data we detect 566 galaxies out of the 671 galaxies in the CFGRS catalog and 317 galaxies out of the 477 galaxies with $I_c < 26$ and at $z < 4.5$ in the photometric redshift catalogue. Most of the galaxies in the

CFGRS catalog, which have no counterpart in our image, are located outside of our final image (between CCD chips or in the masked regions). Galaxies listed in the catalog by Fernández-Soto et al. (1999), but not in our image, are objects fainter than our limiting magnitude. In figures 2b and c, we plot the colors ($I_c - z'$ and $V - I_c$) of the thus-identified galaxies at $z < 4.5$ in the CFGRS sample and in the photometric redshift sample, respectively.

Considering the distribution of the foreground galaxies in the two-color diagrams, we adopt the selection criteria for galaxies at $z \sim 5$ as

$$V - I_c \geq 2.0 \tag{1}$$

and

$$V - I_c \geq 7(I_c - z') - 0.1. \tag{2}$$

The selection window defined by these criteria is shown as the hatched region in figure 2. There is no galaxy in the selection window in the spectroscopic redshift database with $z < 4.5$, and only two galaxies in the photometric redshift database estimated to be at $z < 4.5$. These two galaxies are HDF 3−0238.0 and HDF 4−0505.1. The I_c magnitude of HDF 3−0238.0 in our image is 24.8 mag, and its position in the two-color diagram is close to the boundary of our selection criteria. It is classified as an elliptical galaxy at $z = 0.92$ by Fernández-Soto et al. (1999) and has a round shape both in drizzled HDF-N image and in our I_c-band image. The estimated redshift of HDF 4−0505.1 by Fernández-Soto et al. (1999) is 1.44. It is associated with a more extended object, HDF 4−0505.0, for which the photometric redshift is not available, and it has similar colors to HDF 4−0505.1. Our I_c-band image cannot resolve these two objects. These objects could be interlopers which happen to enter our color selection window.

In figures 2d–f, the color distribution of all of the detected objects is shown. For objects which were not detected in the V-band, we assigned the lower limit of $V - I_c$ color using the limiting V magnitude of 28.5 mag. We regarded such objects (detected in I_c and z'-bands, but not in V-band) as candidates at $z \sim 5$, if they entered the selection window. There are objects with $V - I_c$ and $I_c - z'$ colors whose colors do not match any type of model galaxies or stars. For example, about 4% of all objects have $I - z' < -0.1$. The fraction of such objects with blue $I - z'$ color increases in fainter magnitude. Although some of their colors may be affected by emission lines, we suppose that most of them have redder intrinsic colors, but show the blue colors due to photometric errors.

Among the 35362 detected sources, 321 objects with $I_c \leq 25.5$ fall within this selection window. There are 11 objects with $20.0 < I_c < 23.0$. Most of them lie very close to the boundary of our color selection criteria, and seven objects have neighbours within $5''$. All of them are clearly visible in our V-band image and have round shapes, suggesting that they are elliptical galaxies with old stellar population at intermediate redshift. They are also unusually luminous if they are star-forming galaxies located at $z \sim 5$ (absolute UV magnitude would be $\lesssim -22$).

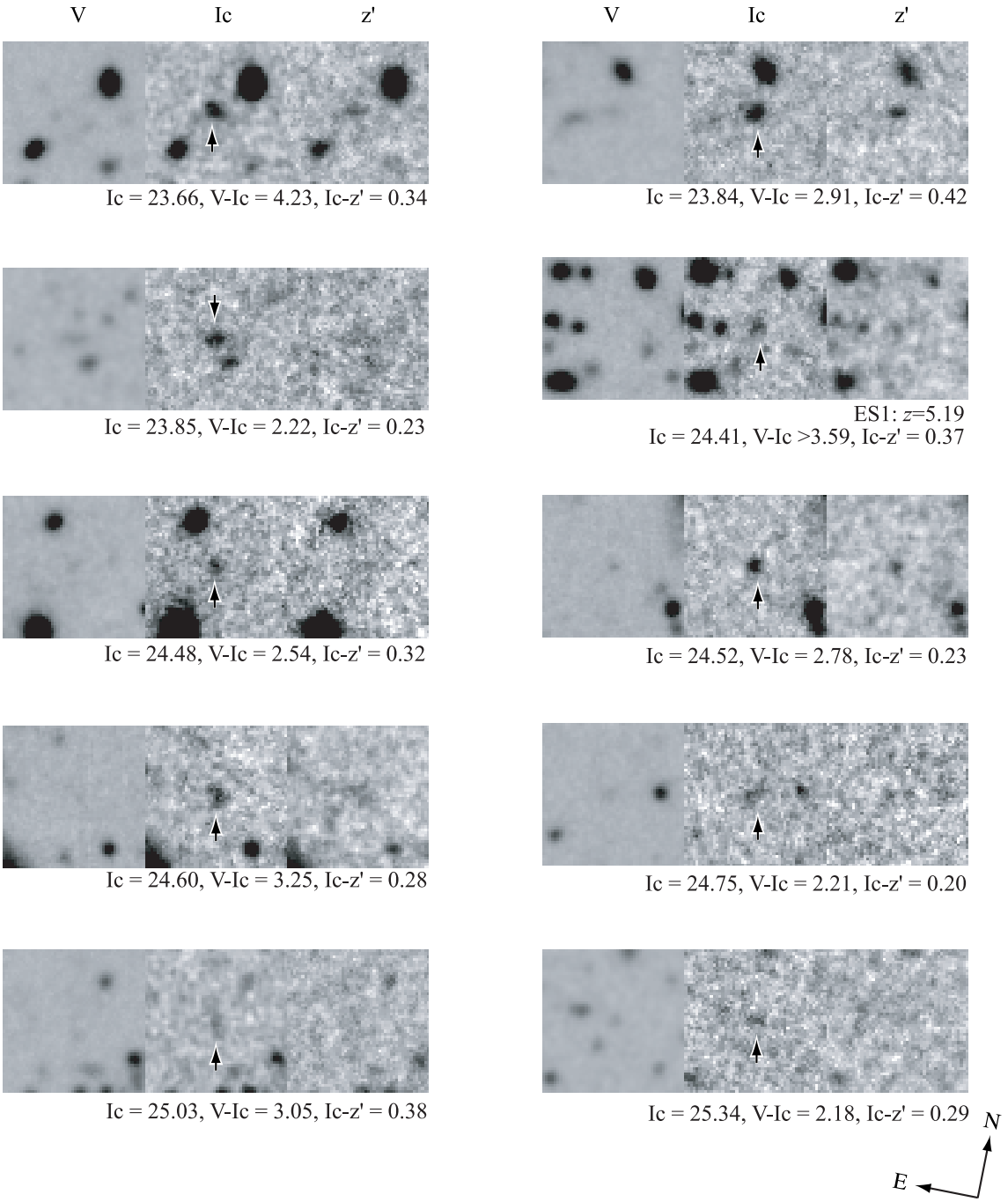

Fig. 3. Images of the representative LBG candidates in an order of I_c magnitude. From left to right, V, I_c, and z'-band images are shown in each panel. The field of view is $10''$.

We regard them as the interlopers which happen to fall within our color selection criteria due to photometric error and excluded them from our candidate list. In figure 3, we show V, I_c, and z'-band images of the representative objects in our LBG candidates in an order of I_c magnitude.

3.2. Cross-Identification with Galaxies in the HDF-N and Its Flanking Fields

We find six LBG candidates in the HDF-N region. The range of the I_c magnitude of these objects is from 24.6 to 25.4. One object, HDF 4−625.0, is spectroscopically confirmed to be at a redshift of 4.58, and for three objects photometric redshifts are provided by Fernández-Soto et al. (1999). The appearances of these four objects with redshift information in the HDF-N drizzled images, as well as in the Suprime-Cam images, are shown in figure 4. Among the three objects for which photometric redshifts are given, two galaxies (HDF 3−238.0 and HDF 4−505.0) have estimated redshifts of 0.92 and 1.44, respectively. Because the objects were detected in the B_{450}-band, they would be interlopers. The other object HDF 3−153.0, which appears to be a single object in our ground-based image, was identified as two resolved objects by Fernández-Soto et al. (1999); one object has a redshift of 1.24 and the other 5.32. Since the latter object is 0.9 mag brighter than the former in I_{814}-band, the detection by our selection criteria is presumably attributed to the object at a higher redshift. As we describe in the next section, the fraction of interlopers at this magnitude range is expected to be around 40 to 50 %. Thus, it is not surprising that half of the objects with redshift information seem to be interlopers. The remaining two objects lie close to the edges of the HDF-N and photometric redshift measurement is not performed on them.

In the flanking fields of the HDF-N we find 12 LBG candidates. Two galaxies have been previously identified spectroscopically as objects at $z \sim 5$. They are J123649.2+621539 (ES1), a serendipitously detected object at $z = 5.19$ (Dawson et al. 2002), and B01−174, a broad-line AGN at $z = 5.186$ discovered in the Chandra Deep Field North region by Barger et al. (2002). The images of ES1 are shown in figure 3.

Vice versa, there are 7 galaxies in the HDF-N and its flanking fields, which have been spectroscopically identified as $4.4 < z < 5.5$ but are not included in our candidate list.[3] One object is located close to the edge of a CCD chip and the source detection was not executed there. Five galaxies are fainter than our magnitude limit or spatially unresolved with a nearby object in our image. The remaining one object is HDF 4−439.0, of which the redshift is given as 4.54 by Stern and Spinrad (1999). The $V - I_c$ and $I_c - z'$ colors of the object are close to the boundary of our selection criteria, and we would fail to select the object probably due to the photometric error.

The detection rate of our survey for those objects with $I_{\rm AB}(814) \gtrsim 25.0$ with a spectroscopic redshift of between $4.4 < z < 5.5$ in the HDF-N and its flanking field is $\sim$1/3. It is consistent with the incompleteness estimated by the Monte Carlo simulations described in the next section.

---

[3] There are three objects with a spectroscopic redshift larger than 5.5 in the HDF-N and its flanking fields. All of them are faint and not detected in our image. As it is described in the next section, incompleteness of our data gets larger for objects at $z \gtrsim 5.5$.

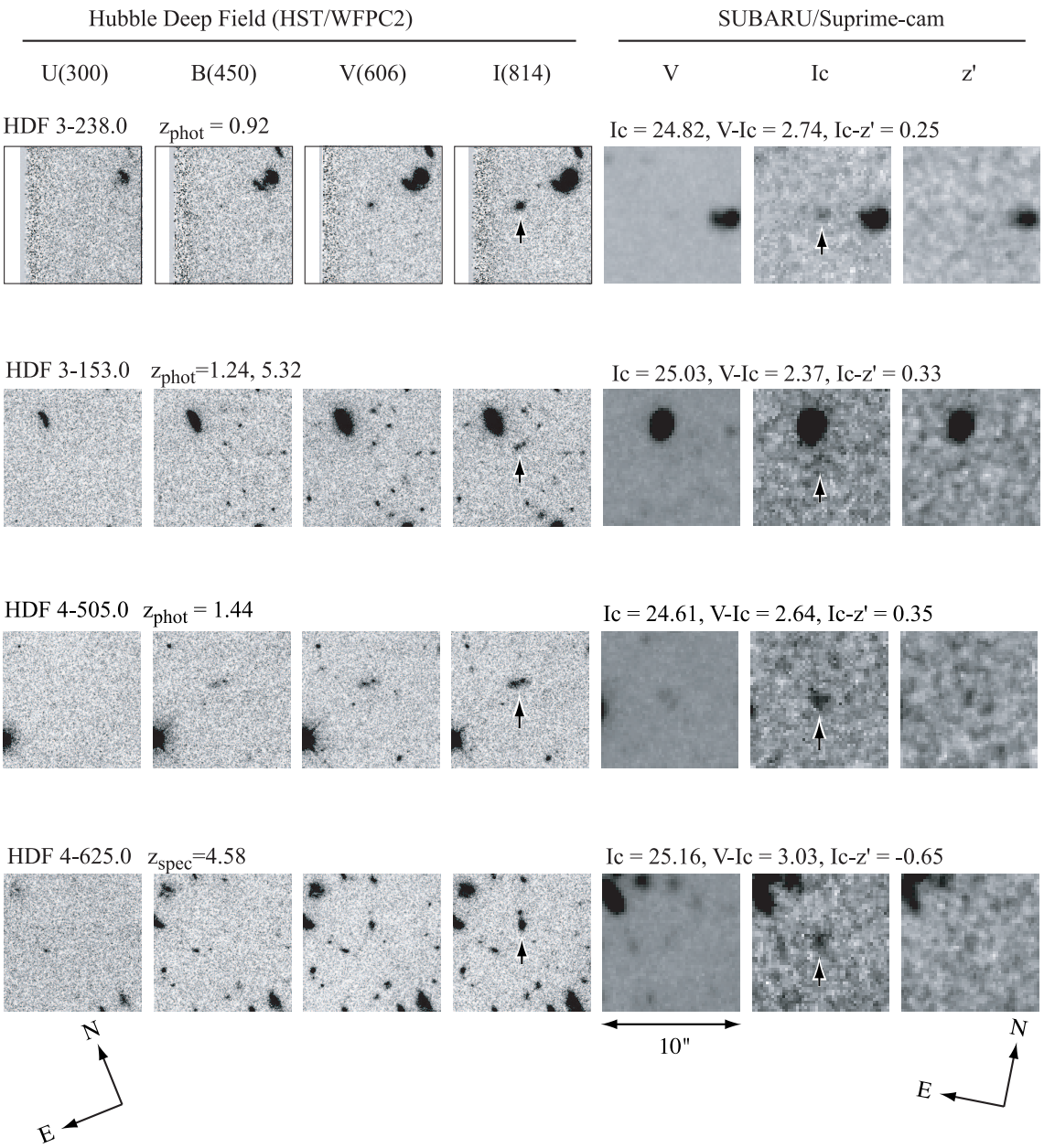

Fig. 4. Images of four LBG candidates in the HDF-N region, of which redshifts (either spectroscopic or photometric) are available. The field of view is 10″. Note that the position angles of the HDF/WFPC2 images and the Suprime-Cam images are different, as shown at the bottom of the figure.

3.3. Morphology and Size Distribution

In regard to the effect of the merging event on the star-formation activity of the LBGs, it is interesting that the HDF-N I_{814} image of HDF 4−625.0 at $z = 4.58$ shows a sign of merging or interaction (see the bottom panels in figure 4). If we can figure out the rate of mergers in our sample, we might be able to assess the effect of merging events on the star formation of the LBGs. Although our ground-based images have poor angular resolution and are not as deep as HDF-N HST/WFPC2 images, we tried to examine the fraction of galaxies showing a sign of interaction with other galaxies among our LBG candidates. We counted the number of objects which have multiple cores in I_c and z'-bands and are not seen or significantly faint in V-band among our LBG candidates with an I_c magnitude of between 24 and 25 (an example is the object with $I_c = 24.60$ in figure 3). Roughly, 10% of the LBG candidates show such a feature. This fraction should, however, be regarded as being a lower limit, since we cannot distinguish close encounters and mergers from a single object. The seeing condition of our observation ($\sim 1''$, corresponding to $\sim 4.4\ h^{-1}$ kpc for $z = 5.0$, $\Omega_{\rm M} = 0.3$, and $\Omega_\Lambda = 0.7$) is not suitable for a detailed analysis of the sizes and morphologies of the LBG candidates; about 40% of the candidates have a half light radius comparable to the seeing size.

3.4. Magnitude and Color Distribution

In figure 5, the apparent I_c magnitudes against the color ($I_c - z'$) are plotted. A tendency that bright blue candidates are deficient can be seen. No other clear trends are seen, though the photometric error is larger for faint objects ($\sim$0.45 mag in $25 < I_c < 25.5$). Figure 6 shows the distribution of $I - z'$ colors of LBG candidates with $I_c \leq 25.0$ in our search. The $I_c - z'$ color of 0.07 mag corresponds to the bluest model LBG spectrum which we adopted in subsection 2.1, which is regarded here as the extinction-free template LBG spectrum. If the redder $I_c - z'$ colors originate in the internal extinction, we are able to derive a rough estimate of the extinction of each galaxy by comparing with the model spectra with different degrees of extinction. In the upper abscissa of the figure, we indicate the $I_c - z'$ color of the model spectra of LBGs at $z = 5$ with $E(B-V) = 0.0$ to 0.4 assuming the extinction law by Calzetti et al. (2000). As it can be seen in figure 2a, the relationship between the $I_c - z'$ color and the dust extinction depends on the redshift of the object. If we adopt a redshift of 4.8 instead of 5.0, $E(B-V) = 0.0$ corresponds to $I_c - z' \sim 0$. The distribution of $E(B-V)$ of the LBGs at $z \sim 3$, estimated by Steidel et al. (1999), is also shown in figure 6 (dashed curve). The distribution of $E(B-V)$ based on a template fitting for rest-frame UV to optical SEDs of LBGs at $z \sim 3$ (Papovich et al. 2001) is broadly consistent with that of Steidel et al. (1999). Although the photometric errors for fainter objects in our candidates are large, and a possible contamination by the emission lines might disturb this distribution, the degree of dust extinction for LBG candidates detected by our search seems to be similar to those at $z \sim 3$.

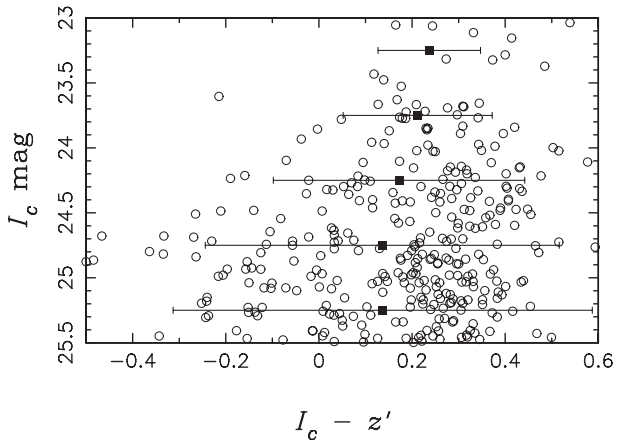

Fig. 5. Apparent I_c magnitude against the $I_c - z'$ color for LBG candidates at $z \sim 5$. The mean values of the $I_c - z'$ colors in 0.5 I_c mag step are shown by the filled squares. Each error bar represents the photometric error of the $I_c - z'$ color in each 0.5 magnitude bin, measured by a simulation using artificial objects (see subsection 2.4).

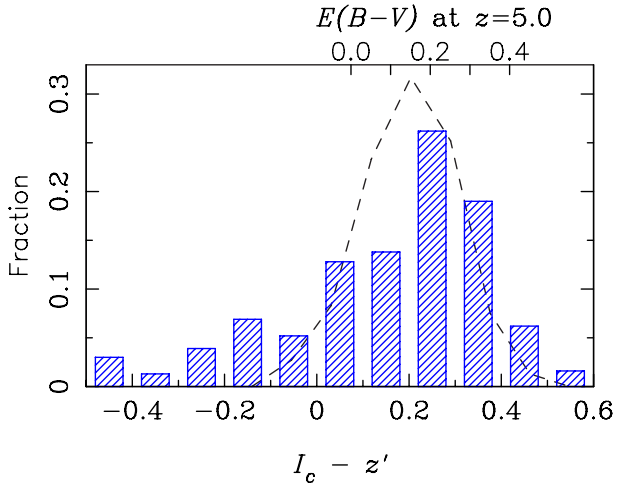

Fig. 6. $I_c - z'$ color distribution of LBG candidates at $z \sim 5$. The objects with $I_c - z'$ colors less than -0.5 are included in the bin for the bluest color. The ticks at the upper horizontal axis indicate the expected $I_c - z'$ colors of a model galaxy at $z = 5$ with $E(B-V)$ from 0.0 to 0.4. See text for the details. The dashed line shows a distribution of $E(B-V)$ for LBGs at $z \sim 3$ by Steidel et al. (1999).

4. Luminosity Function of the LBG Candidates at $z \sim 5$

In this section, we try to derive a luminosity function of LBGs at $z \sim 5$ *statistically* using our LBG candidates. The redshifts of the candidates are not yet confirmed by spectroscopy, except for a few objects. However, considering that the method works so efficiently at $z \sim 3$ and $z \sim 4$, and the color selection criteria adopted here is well examined thanks to a large redshift database based on deep spectroscopic and multi-waveband photometric observations in HDF-N and its flanking fields, we believe that the catalog is reliable enough to discuss their statistical nature. We would like to make a follow-up spectroscopy in the future, but it would take many years. Under these circumstances, constructing luminosity function and discussing its implication to cosmic star-formation history statistically is opportune at this stage. In deriving the luminosity function of the LBGs at $z \sim 5$, we should consider two important issues: Contamination by interlopers and incompleteness of the sample. In the following procedure of this section we exclude the data in the CCD chip at the south-west corner with many bad columns; only five candidates are detected in the chip.

4.1. Correction for Contamination by Interlopers

In section 3 it has been described that our selection criteria are defined to be least contaminated by interlopers via redshift database of galaxies in the HDF-N and its flanking fields. While the galaxies in the HDF-N and its flanking fields are quite useful for determining the selection criteria, they are not suitable for estimating the number of interlopers contained in our LBG candidates, because the number of these galaxies with the available redshift is only a few per cent of all the detected sources in our survey. Thus, an estimation of the contamination rate based on the whole sample of the detected objects in our catalog is necessary for a proper correction for interlopers.

There are some possible causes of contamination by interlopers other than photometric errors: the first one is interlopers with colors which are intrinsically similar to LBGs at $z > 4.5$, and the second one is systematic errors due to the indirect z'-band calibration (subsection 2.3). The fact that there is no object at intermediate redshift for galaxies in the CFGRS and only two among 317 galaxies in the photometric redshift catalog of HDF-N by Fernández-Soto et al. (1999) (see subsection 3.1 and figures 2b and c) would certify the validity of our selection criteria [equations (1) and (2) in subsection 3.1]. This estimation of contamination by interlopers described below is based on this assumption. In regard to the systematic error due to the z'-band calibration, it does not affect our results, because we have defined our color selection criteria based on the colors of galaxies at the intermediate redshift in the HDF-N and its flanking fields. If $I_c - z'$ color distribution is shifted due to the systematic zero point shift in z'-band, the color selection criteria should also be shifted in the same direction. So we only consider photometric errors in quantifying the degree of contamination below.

The fraction of interlopers varies with their apparent magnitude, because the larger

photometric errors in the measurement of fainter objects should increase the probability of their invasion into the $z \sim 5$ selection window, even if their intrinsic color is the same as the brighter ones. Thus, we should estimate and correct the fraction of interlopers at each magnitude bin. In order to accomplish this task, we employed a resampling (bootstrap) algorithm. First, we selected objects at the outside of the selection window in the $V - I_c$ and $I_c - z'$ color diagram from all of the detected objects. We then divided them by their I_c magnitude with a 0.5 mag step. For each magnitude bin, we resampled objects randomly while allowing the possibility of duplication. The number of objects included in a resampled group was the same as the number of objects in the magnitude bin. We then assigned photometric errors to $V - I_c$ and $I_c - z'$ colors according to the observed I_c magnitude and the color of each object; i.e., according to the V and z'-band magnitudes. The error values in each band were based on the estimation by putting many artificial objects, and the obtained error values are consistent with those estimated from the background noise with a $1\farcs6$ diameter (see subsection 2.4). The typical values for objects with colors close to the border of our color selection criteria were 0.07 mag and 0.11 mag for $V - I_c$ and $I_c - z'$ colors, respectively, for objects with $23.0 < I_c \leq 23.5$, and 0.43 mag and 0.45 mag for $V - I_c$ and $I_c - z'$ colors, respectively, for objects with $25.0 < I_c \leq 25.5$. The error assignment was made randomly under the assumption that photometric errors have a Gaussian distribution. We counted the number of objects of which modified colors are in the selection window. We ran this procedure 1000 times for each magnitude bin, and regarded the average of the numbers of objects that fall in the selection window as being the estimated number of interlopers. We also performed the same procedure by adding objects which are placed inside of the selection window, but are close to the boundary; their color differences from the boundary of the selection criteria are within the photometric errors in both $V - I_c$ and $I_c - z'$. By this test we intended to estimate the possible maximum number of interlopers. The number of objects within the window after adding the random error was roughly twice the number which resulted in the first test (in which the objects at the outside of the selection window were used) over the all magnitude ranges. Since some (not all, but unknown) fraction of the objects within the selection window is considered to be interlopers, the first test should underestimate the number of interlopers, while the second test should overestimate it. We took the average of the results of these two tests as the expected number of interlopers. The variation in the number densities caused by this uncertainty in the estimation of the interlopers is $\sim$ 10–30% for all magnitude bins. We show the number of the interlopers thus obtained in table 2. The estimated fraction of interlopers gradually increases along with the magnitude, from 22% at $23.0 < I_c < 23.5$ to 48% for $25.0 < I_c < 25.5$. The result is consistent with the fact that no or only a few interlopers are seen for spectroscopic or photometric redshift catalog obtained in the HDF-N and its flanking fields (figures 2b and c), since the area of the HDF-N is smaller than our effective surveyed area by a factor of ~ 100.

Subtraction of these numbers from the numbers of objects within the color selection

Table 2. Number of objects detected in our survey with colors expected for galaxies at $z \sim 5$, and corrections for interlopers, noise misidentification, and incompleteness.

Magnitude range (I_c) (1)	Detected number (2)	Expected number of interlopers (3)	Noise rate* (4)	$N(m)$ [(2)−(3)]×[1−(4)]
23.0–23.5	6	1.3 (22%)	0.0	4.7
23.5–24.0	25	6.6 (26%)	0.0	18.4
24.0–24.5	61	18.5 (30.3%)	0.0	42.5
24.5–25.0	91	33.9 (37.3%)	0.036	55.0
25.0–25.5	122	58.5 (48.0%)	0.172	52.6

* Fraction of misidentification of noise as an object, estimated by the cross-identification with the HDF-N catalog.

window gives the expected numbers of objects at $z \sim 5$ if there is no contamination of noise. As described in subsection 2.4, a cross-identification of the sources with the HDF-N catalog shows that in the magnitude range $I_c \leq 24.5$ the sources are almost noise-free. In the fainter magnitude range, we have to multiply the expected number (difference of the values in columns 2 and 3 in table 2) by the fraction of the real objects among the total list of detected sources (1 minus the values in the fourth column in table 2), because the fraction of noises for the detected sources outside of the color selection window must be the same as that in the window. Accordingly, we obtain $N(m)$, the corrected number of objects at $z \sim 5$ in a magnitude range between $m \pm 0.25$.

4.2. Correction for Incompleteness

The other thing that we have to consider for a proper derivation of the luminosity function is a correction for the incompleteness of our survey. We should consider two aspects of incompleteness (Steidel et al. 1999). One is the detection rate against the magnitude; the detection rate decreases with increasing magnitude, which is the usual detection incompleteness. The other one is the rate against the redshift and color; as can be seen in figure 2a, at a redshift range of around 4–4.5, the detection rate should strongly depend on the color of an object. In addition, at higher redshift (say $z > 5.5$), the location of the detected sources in figure 2 goes out of the window when they are fainter than the detection limit in the V-band.

In order to correct these incompleteness, we ran Monte Carlo simulations. These Monte Carlo simulations enabled us to calculate the "effective volume" of our survey (Steidel et al. 1999),

$$V_{\rm eff}(m) = \int dz p(m,z) dV/dz, \tag{3}$$

where $p(m,z)$ is the probability of finding an object with a magnitude of m at a redshift of z, which can be obtained as the average weighted over the distribution of SEDs of LBGs.

First, we created sets of artificial objects with various magnitudes and colors at various redshifts. The number of objects created in each set was 200. The magnitude range was taken from 23 mag to 25.5 mag with a 0.5 magnitude bin. Their angular sizes were adjusted so that the obtained size distribution of the model objects resembled that of real objects at the same magnitude. Their $V - I_c$ and $I_c - z'$ colors of LBGs at $z = 4.0 - 5.9$ were calculated using the model spectra reproducing those of LBGs described in subsection 2.1. The redshift step was 0.1. We took objects with five different colors, which corresponded to $E(B-V)$ of 0.0, 0.1, 0.2, 0.3, and 0.4 for each redshift and magnitude using the model SEDs. Thus, we created $5 \times 20 \times 5 = 500$ sets of 200 artificial objects for each of 8 CCDs. Then we put these artificial objects into our V, I_c, and z'-band images with a random spatial distribution, and performed object detection in the same way as we did for real objects. Next, we counted the number of detected objects which fell in our selection window for $z \sim 5$ objects. The fraction of the objects which satisfied our color selection criteria can be regarded as the probability of detecting an object with the magnitude and color at a certain redshift. A weighted average of the probabilities was calculated using the $E(B-V)$ distribution of LBGs at $z \sim 3$ by Steidel et al. (1999) within the range of $E(B-V) = 0.0$–0.4 (see dashed curve of figure 6). As described in subsection 3.4, the $E(B-V)$ distribution of our LBG candidates is suggested to be similar to that by Steidel et al. (1999). The resulting probability, $p(m, z)$, averaged over 8 CCD chips is shown in figure 7.[4] The overall decrease in detection rate along the magnitude is clearly seen. At a lower redshift ($z = 4$–4.5), the detection rate decreases because of the cutoff of the selection window; the degree of the decline depends on the color, and thus the color distribution of LBGs. At a higher redshift ($z = 5.2$–5.6), the detection rate decreases because the sources detected in the I_c-band, but not in the V-band, go out of the selection window at a fainter I_c magnitude and at a redder $I_c - z'$ color. The sum of the effective volumes of 8 CCD chips obtained for each magnitude range is summarized in table 3 for the two cosmological models.

4.3. Luminosity Function at $z \sim 5$

The information concerning the contamination of the interlopers and the incompleteness of our search described in the previous two subsections allow us to calculate the luminosity function of the Lyman break galaxies at $z \sim 5$ as

$$\Phi(m) = N(m)/V_{\rm eff}(m), \tag{4}$$

where $N(m)$ is the number of objects in a magnitude bin of m corrected for the estimated contamination by interlopers and noise. The thus-derived luminosity function is that at rest UV 1340 Å, which redshifts into the central wavelength of the I_c-band (8060 Å) for a redshift of 5. In order to compare it with the luminosity functions at $z \sim 3$ and $z \sim 4$ obtained by Steidel et al. (1999), we calculated the absolute AB magnitudes at 1700 Å and derived the

[4] The variation of $p(m, z)$ among 8 CCD chips is not large; the variation of the $V_{\rm eff}$ obtained by equation (3) for each CCD is a few % for the bright ($23.0 < I_c \leq 24.0$) sources, and $\sim 35\%$ for the faintest sources.

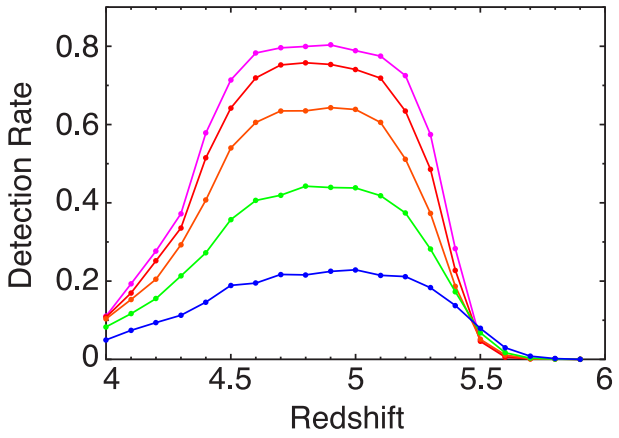

Fig. 7. Detection rate $p(m,z)$ of the galaxies against the redshift of the objects estimated based on Monte Carlo simulations. Each line indicates the detection rate for an I_c magnitude range of 23.0–23.5, 23.5–24.0, 24.0–24.5, 24.5–25.0 and 25.0–25.5 (from top to bottom).

Table 3. Number densities of LBG candidates at $z \sim 5$.

Magnitude		$\Omega_{\rm M} = 0.3$, $\Omega_\Lambda = 0.7$		
range (I_c)	$n(m)^*$	$M_{\rm UV}({\rm AB})^\dagger - 5\log h$	$V_{\rm eff}^\ddagger$	$\log \Phi(m)^\S$
23.0 – 23.5	0.82± 0.41	−22.1 – −21.6	741.32	−4.65
23.5 – 24.0	3.20± 0.93	−21.6 – −21.1	679.07	−4.03
24.0 – 24.5	7.39± 1.83	−21.1 – −20.6	565.47	−3.58
24.5 – 25.0	9.57± 2.10	−20.6 – −20.1	388.65	−3.31
25.0 – 25.5	9.14± 2.79	−20.1 – −19.6	204.31	−3.05

Magnitude		$\Omega_{\rm M} = 1.0$, $\Omega_\Lambda = 0.0$		
range (I_c)	$n(m)^*$	$M_{\rm UV}({\rm AB})^\dagger - 5\log h$	$V_{\rm eff}^\ddagger$	$\log \Phi(m)^\S$
23.0 – 23.5	0.82± 0.41	−21.2 – −20.7	174.01	−4.02
23.5 – 24.0	3.20± 0.93	−20.7 – −20.2	159.40	−3.40
24.0 – 24.5	7.39± 1.83	−20.2 – −19.7	132.74	−2.95
24.5 – 25.0	9.57± 2.10	−19.7 – −19.2	91.21	−2.68
25.0 – 25.5	9.14± 2.79	−19.2 – −18.7	47.94	−2.42

* Surface number density of LBG candidates in 10^{-2} arcmin^{-2} per 0.5 mag. These are derived by dividing $N(m)$ in table 2 by the effective surveyed area (575.0 arcmin^2).

† Absolute magnitude in ABmag [$I_c({\rm AB}) = I_c({\rm Vega}) + 0.45$], calculated from I_c magnitude by assuming the redshift of 5.0 for all the objects.

‡ Effective volume of our survey in the unit of h^{-3} Mpc^3 arcmin^{-2}.

§ Number density of the $z \sim 5$ LBG candidates in the unit of h^3 mag^{-1} Mpc^{-3}.

luminosity function at the wavelength, assuming a flat spectrum (in f_ν) which corresponds to $I_c - z'$ color of 0.1 mag in the Vega magnitude system. Table 3 gives the number density of the LBG candidates in the 0.5 mag step corrected for the incompleteness and the contamination. The luminosity function of the $z \sim 5$ population is presented as red circles in figure 8. In deriving the luminosity function, we assumed a redshift of 5.0 for all of the LBG candidates to calculate their luminosity distance. If we used a weighted mean redshift of 4.8 derived from $p(m, z)$ (see figure 7) instead, the absolute magnitude became 0.10 mag fainter than that at $z = 5.0$. In order to show how much the corrections for contaminations and incompleteness affect the luminosity function, we show two alternative number densities with solid squares and triangles in figure 8. The solid squares represent the number density of LBGs at $z \sim 5$ in the case that the correction for contamination is skipped; i.e., all objects match with our color selection criteria are assumed to be genuinely at $z \sim 5$. The solid triangles indicate the number density assuming that the detection rate is 1.0 within a redshift range between 4.4 and 5.2, and otherwise 0 for all of the magnitude range instead of using the detection rates estimated by the Monte Carlo simulation shown in figure 7. In figure 8 we also show the luminosity functions for $z \sim 3$ and 4 obtained by Steidel et al. (1999) as open circles and open triangles. In deriving these luminosity functions, Steidel et al. (1999) assumed $\langle z \rangle = 3.04$ and $\langle z \rangle = 4.13$, respectively, according to the results of their spectroscopic observations.

There is no significant difference between the luminosity functions for $z \sim 3$, 4, and 5 in the bright part. Although the change of the adopted cosmology makes a slight difference in the relative position of the data points, the general tendency remains in both figures. In the fainter part, there is a hint of a decrease in the number density at $z \sim 5$. It should be worth noting here that in figure 8, while the vertical error bars for our $z \sim 5$ data include errors in the corrections for interlopers and incompleteness, as well as statistical errors in the number of the candidates assuming a Poisson distribution, the error bars for $z \sim 3$ and 4 by Steidel et al. (1999) only include statistical errors. Since the incompleteness of the $z \sim 3$ survey is reported to be comparable to, or slightly better than, ours (Steidel et al. 1999), if the uncertainty in the corrections for incompleteness and contamination of the interlopers are considered, the error bars for $z \sim 3$ data points should be larger than those appearing in figure 8. Thus, within the current depth and uncertainties of the observed data it is hard to conclude whether the discrepancy between the number density for $z \sim 5$ and that for $z \sim 3$ at the fainter part is real or not.

Steidel et al. (1999) and Adelberger and Steidel (2000) made a Schechter function fitting to the luminosity function of LBGs at $z \sim 3$, and derived a set of parameters ($m^* = 24.54$, $\alpha = -1.57$ and $\phi^* = 4.4 \times 10^{-3}$ h^3 mag^{-1} Mpc^{-3}) under the assumption $\Omega_M = 0.3$ and $\Omega_\Lambda = 0.7$. We made an error-weighted Schechter function fitting for our data for $z \sim 5$, and derived $m^* = 24.5$, $\alpha = -1.50$, and $\phi^* = 1.1 \times 10^{-3}$ h^3 mag^{-1} Mpc^{-3}. In figure 9 we show these two Schechter functions overplotted on the observed data points.

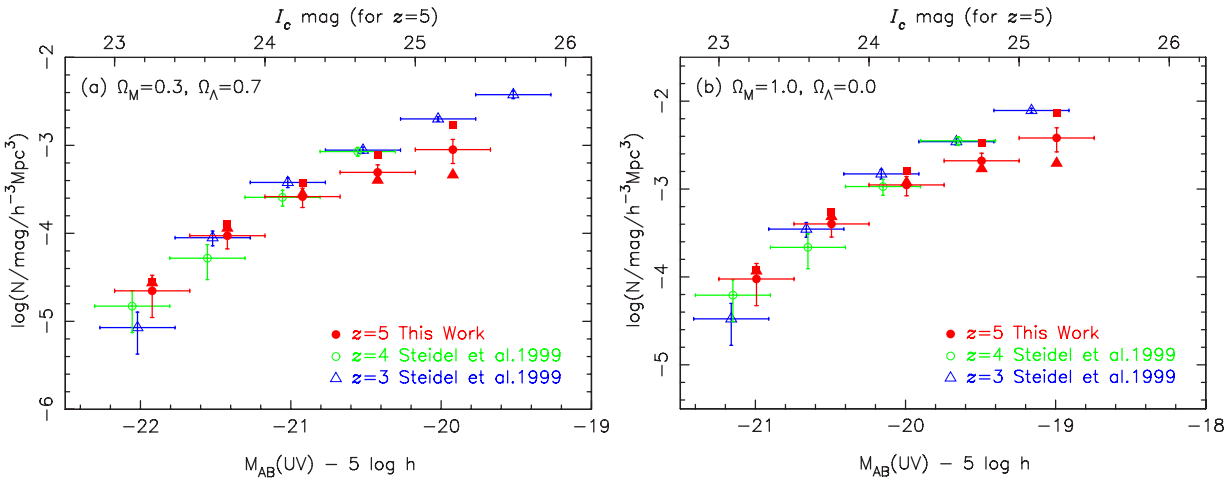

Fig. 8. Luminosity function of the Lyman break galaxies at $z \sim 5$ (red). The assumed cosmology is $\Omega_{\rm M} = 0.3$ and $\Omega_\Lambda = 0.7$ for figure 8a and $\Omega_{\rm M} = 1.0$ and $\Omega_\Lambda = 0.0$ for figure 8b. The vertical error bars for our $z \sim 5$ data include errors in corrections for interlopers and incompleteness, as well as the statistical errors in the number of the candidates assuming the Poisson distribution. The assumed redshift is $z = 5.0$. The horizontal error bars indicate the magnitude step (0.5 mag) for all data points. The solid squares show the luminosity function without a correction for contamination, and the solid triangles are for a simple selection function, which is 1.0 for a redshift range 4.4 to 5.2, and otherwise 0 regardless of the magnitude. The open triangles and open circles represent the luminosity functions of LBGs at $\langle z \rangle = 3.04$ and $\langle z \rangle = 4.13$, respectively, taken from Steidel et al. (1999). The vertical error bars for them only show statistical errors.

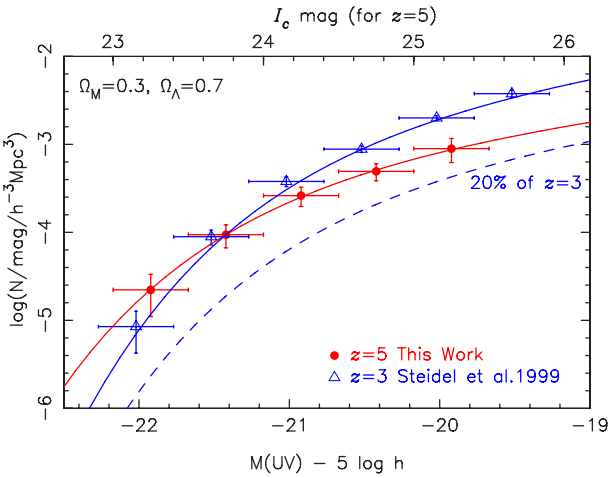

Fig. 9. Same as figure 8a, but only for LBGs at $z \sim 3$ and 5. Schechter functions fitted to the data are also shown. The dashed line indicates a Schechter function with a 20% number density of LBGs at $z \sim 3$. The assumed cosmology is $\Omega_{\rm M} = 0.3$ and $\Omega_\Lambda = 0.7$.

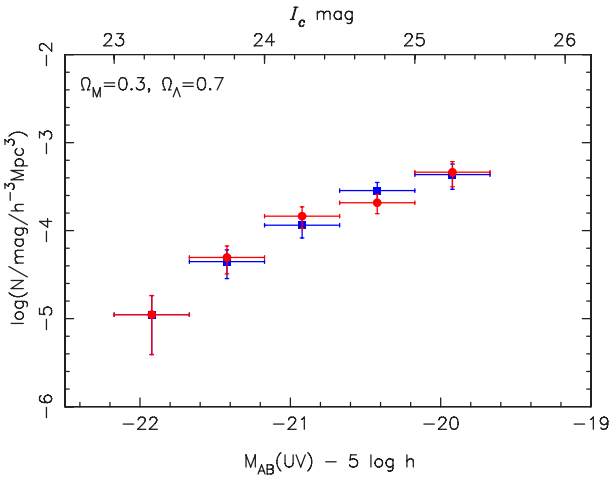

Fig. 10. Luminosity functions of LBGs at $z \sim 5$ with red UV colors ($I_c - z' \geq 0.21$, red points) and blue colors ($I_c - z' < 0.21$, blue points).

Meurer et al. (1999) suggested the existence of a correlation between the rest-frame UV color and luminosity of the LBGs at $z \sim 3$; bright LBGs tend to be red. Ouchi et al. (2001b) reported that the number density of LBGs at $z \sim 4$ shows an excess of bright red galaxies, which is qualitatively consistent with the result by Meurer et al. (1999). In order to see whether such a correlation between the UV color and the luminosity exists in our sample, we divided it into two subsamples based on their $I_c - z'$ colors (rest-frame 1340–1520 Å) at the median value of 0.21 mag; we show their luminosity functions in figure 10. In the bright part, the number density of the red galaxies ($I_c - z' \geq 0.21$) is slightly larger than that of the blue galaxies. This trend can also be seen in figure 5. However, the correlation between the luminosity and the color is not as clear as in Ouchi et al. (2001b), who performed the same procedure for their LBG candidates at $z \sim 4$, and found that red objects are more than two-times as abundant in the brighter part of the luminosity function. For objects with $I_c \leq 24.5$ in our sample, the number of red galaxies is ~ 1.14 times more than that of blue galaxies. Although these results do not conflict with the results by Meurer et al. (1999) and Ouchi et al. (2001b), the correlation of the UV color and the luminosity in our $z \sim 5$ sample seems to be weaker than those at $z \sim 3$ and $z \sim 4$.

5. Discussion

5.1. Star-Formation History of an Individual LBG

Our results show that the luminosity function of LBGs at $z \sim 5$ is similar to those at $z \sim 3$ and at $z \sim 4$, though there may be a slight evolution in the faint part. Does this imply that the LBGs at $z \sim 5$ are the same LBGs as at $z \sim 3$? Are they continuously forming stars during the period from $z \sim 5$ to $z \sim 3$ (~ 1 Gyr in our adopted Λ cosmology)? Shapley et al. (2001) derived the ages of LBGs at $z \sim 3$ by the model SED fitting method assuming constant star formation.

They found that the median age is 320 Myr and that many have ages of less than 200 Myr, and that only 20% of them have ages greater than 1 Gyr. The fraction of the 20% depends slightly on the luminosity, but there is no clear tendency such as brighter objects have larger ages or vice versa. Therefore, most of the LBGs at $z \sim 3$ were not yet forming stars at $z \sim 5$, and are not direct descendants of LBGs at $z \sim 5$, if we suppose the continuous star-formation history for an individual object. In figure 9 we illustrate this with a Schechter function for a 20% number density of LBGs at $z \sim 3$ as a dashed line, by simply assuming that each object has a continuous and constant star-formation history with an age derived by Shapley et al. (2001). If we compare the number densities in the bright part (say $M_{\rm UV} - 5{\rm log}h \lesssim -21$), the number density for LBGs at $z \sim 5$ is close to that at $z \sim 3$ and the difference is distinct from the 20% line. The same situation is depicted by Ferguson et al. (2002). They also argue that an amount of star-formation density at $z \sim 5$, contributed by the LBGs seen at $z \sim 3$, must be about ten-times smaller than that at $z \sim 3$ for the continuous star-formation history.

If the LBGs at $z \sim 3$ are not the direct descendants of LBGs at $z \sim 5$, did the LBGs at $z \sim 5$ stop star formation by $z \sim 3$? Do they fade out at $z \sim 3$? Papovich et al. (2001) point out the absence of massive, non-star-forming galaxies in the HDF-N at $z \sim 3$. It may indicate that the descendants of LBGs at a higher redshift, which have stopped star formation and become fainter in UV by $z \sim 3$, are rare. Alternatively, the assumption of constant star formation may not be appropriate; star formation may be sporadic. In this case, the ages derived by the SED fitting method would be taken to be those of the most recent starburst. Papovich et al. (2001) tested SED fitting using two-component models comprising old and young stellar populations, and claim that the two-component fitting generally gives smaller ages for the young population than the single-age models. The sporadic star formation and the short duty-cycle of the starburst would naturally explain the small ages of young stellar population and the existence of older stellar component as well as the similarity of the UV luminosity functions at $3 \lesssim z \lesssim 5$. Supposing the sporadic star-formation history for an individual galaxy seems to be reasonable, because the hierarchical clustering model generally implies that a merging process must occur for LBGs at high redshift. In this case, a burst of star formation may occur during a merging or a galaxy interaction. In fact, Nagamine (2002) showed that such a sporadic star-formation history for each galaxy takes place associated with a merging in a large-scale hydrodynamic simulation. He also presents a resultant rest-frame V-band luminosity function at $z = 5$. We compare it with our result in the UV, assuming a $UV - V$ color of the model template spectrum with a moderate reddening. Although the model luminosity function gives a good agreement with the number density of LBGs at the bright part, it shows a significant excess ($\sim$1 dex) in the fainter part. However, a color could depend on the luminosity, and this comparison seems to be premature; we need to compare our result with a model luminosity function directly derived at UV.

5.2. Evolution of the UV Luminosity Density

We can calculate the UV luminosity density at $z \sim 5$ by integrating the obtained luminosity function. In this calculation the integration is made in the magnitude ranges of $23.0 < I_c \leq 25.0$ and $23.0 < I_c \leq 25.5$. The I_c magnitudes of 23.0 and 25.5 approximately correspond to $M_{\rm UV} - 5{\rm log}h$ of -22.5 and -20.0 in the Λ-cosmology and -21.7 and -19.2 in the Einstein–de Sitter cosmology, respectively. The former integration range is chosen to match with the limiting magnitude of the $z \sim 4$ sample by Steidel et al. (1999) in terms of the absolute magnitude. The results are listed in table 4, together with those of $z \sim 3$ and $z \sim 4$ by Steidel et al. (1999). As it is expected from the shape of the luminosity function in particular at faint part, the resultant UV luminosity density at $z \sim 5$ is 0.56–0.69 times of that at $z \sim 3$ in the same absolute magnitude range, depending on the choice of cosmology and the integration range. The UV luminosity density seems to becoming smaller at a higher redshift, though the difference between $z \sim 5$ and $z \sim 3$– 4 is comparable to the uncertainty, and we cannot rule out the possibility that the UV luminosities are almost constant at this redshift range. Madau et al. (1996, 1998) derived the UV luminosity densities at $2 \lesssim z \lesssim 4$ using LBGs in the HDF-N. Their values are smaller than those by Steidel et al. (1999) by a factor of 2–4. The search field for LBGs by Madau et al. (1996, 1998) is much smaller than that by Steidel et al. (1999), and the discrepancy may originate in the small search volume in the HDF-N due to the cosmic variance (Steidel et al. 1999). Casertano et al. (2000) also found a 1.3–1.9 times higher UV luminosity density at $2 \lesssim z \lesssim 4$ in the HST/WFPC2 image of HDF-S, as compared with that in the HDF-N.

To examine the degree of uncertainty in deriving the UV luminosity density, we made a calculation of the luminosity function and the UV luminosity density using smaller numbers of interlopers (the first test described in subsection 5.1). The resulting UV luminosity density is $\sim$ 1.2-times larger than those listed in table 4 (an increase of 0.08 in log scale). In addition, there is also an uncertainty in the estimate of the effective volume. From the chip-to-chip variation, the uncertainty of the effective volume for the whole survey area is estimated to be $\sim 10\%$. Taking these two uncertainties into account, the upper most possible UV luminosity density is estimated to be about 1.6-times (~ 0.2 dex) larger than that given in table 4. The value is comparable to the luminosity densities at $z \sim 3$ listed in table 4.

In figure 11 we show the star-formation density as a function of the redshift. The assumed cosmology is $\Omega_{\rm M} = 0.3$ and $\Omega_\Lambda = 0.7$. The data point at $z \sim 5$ from our data and the points at $z \sim 3$ and 4 from Steidel et al. (1999) are derived by integrating the observed number densities for objects down to $M_{\rm UV} - 5{\rm log}h \lesssim -20$, as listed in table 4. For these data points at $z \gtrsim 3$, the UV luminosity density at 1500 Å is converted to the star-formation density using a conversion factor by Madau et al. (1998), i.e., SFR ($\rm M_\odot\ yr^{-1}$) = $L_{\rm UV}$ (erg $\rm s^{-1}$ $\rm Hz^{-1}$) $\times 1.25 \times 10^{-28}$. For $z \sim 5$ data point this gives SFR of 7.18×10^{-3} h $\rm M_\odot\ yr^{-1}$ $\rm Mpc^{-3}$ (-2.14 in log scale) and 1.30×10^{-2} h $\rm M_\odot\ yr^{-1}$ $\rm Mpc^{-3}$ (-1.88 in log scale) for the Λ cosmology and

Table 4. UV luminosity densities.

	log $\rho_{\rm UV}$ [h erg s^{-1} Hz^{-1} Mpc^{-3}]*			
	$\Omega_{\rm M}=0.3$, $\Omega_\Lambda=0.7$		$\Omega_{\rm M}=1.0$, $\Omega_\Lambda=0.0$	
Redshift	$M_{\rm UV}-5\log h \lesssim -20.5$	$M_{\rm UV}-5\log h \lesssim -20.0$	$M_{\rm UV}-5\log h \lesssim -19.7$	$M_{\rm UV}-5\log h \lesssim -19.2$
$z=3^\dagger$	25.75±0.07	25.97±0.07	26.05±0.07	26.27±0.07
$z=4^\dagger$	25.70±0.10 (89%)	···	25.96±0.10 (81%)	···
$z=5$	25.59±0.11 (69%)	25.76±0.16 (62%)	25.85±0.11 (63%)	26.02±0.16 (56%)

* UV luminosity density is obtained directly from the integration of the observed number densities. Values shown in parentheses are percentage of the UV luminosity density relative to that at $z\sim3$.

† Steidel et al. (1999).

the Einstein–de Sitter cosmology, respectively. The data points for $z\sim0.5$–2.0 are taken from Connolly et al. (1997), which is based on the UV luminosity densities at a rest-frame of 2800 Å. For this wavelength we adopt a conversion factor, SFR ($M_\odot$ yr^{-1}) = $L_{\rm UV}$ (erg s^{-1} Hz^{-1}) $\times1.27\times10^{-28}$, also given by Madau et al. (1998). Originally, their UV luminosity densities are given by integrating the Schechter UV luminosity function over the total luminosity range, and a calculation is made for the Einstein–de Sitter universe. We adopt here a Schechter function with $\alpha=-1.3$, and for consistency with the data at $z\geq3$, the integration of the UV luminosity function is made down to $M_{\rm UV}-5{\rm log}h=-20$. The correction for different cosmological parameters is made following the prescription by Somerville et al. (2001). In figure 11 we also indicate the star-formation density with a simple dust extinction correction as open symbols. In correcting dust extinction we follow Steidel et al. (1999), who used the extinction curve by Calzetti et al. (2000) and assumed $E(B-V)=0.15$ for all data points. As Steidel et al. (1999) have remarked, the validity of such uniform correction is not clear, since the degree of extinction may be redshift-dependent, and dust properties may change form time to time. As described in subsection 3.4, the $E(B-V)$ distribution estimated from the I_c-z' colors at $z\sim5$ is similar to that of galaxies at $z\sim3$ (figure 6), although the photometric error is large for faint objects. Thus, the assumption that the degree of dust extinction is similar from $z\sim3$ to 5 might not be inconsistent with our observed results for LBGs at $z\sim5$, although there may be heavier dust extinction at $z\sim1$ (Tresse et al. 2002).

We should note that the values of the star-formation density appearing in figure 11 are smaller than those in figure 9 of Steidel et al. (1999). This is because our integration limit of the luminosity function is about 0.5 mag brighter than that of Steidel et al. (1999). The position of the data points for $z\sim1.75$ is about 0.4 dex higher relative to $z\sim3$ in figure 11, while in Steidel et al. (1999) the difference is ~0.2 dex. This is caused by the difference of the adopted slope of the fainter part of the luminosity function between $z<2$ and $z=3$–4.

The overall shape of the star-formation history presented in figure 11 shows a steep rise

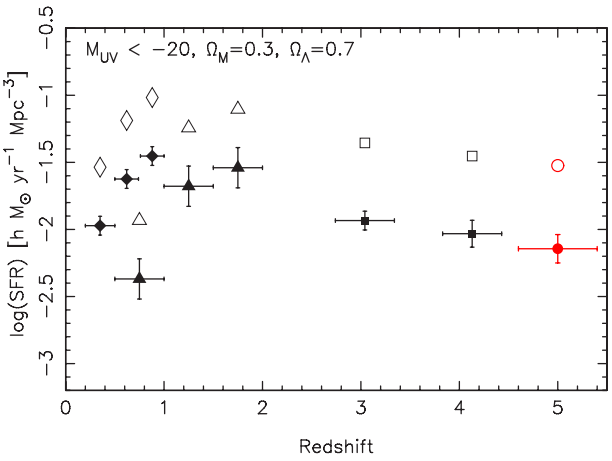

Fig. 11. Star-formation density as a function of the redshift. Our data point for $z \sim 5$ LBGs are marked as a filled circle. Our data and those by Steidel et al. (1999) at $z \sim 3$ and 4 (shown in filled squares) were derived by integrating the luminosity function with the absolute UV magnitude, $M_{\rm UV} - 5 \log h \lesssim -20.0$ (see table 4). The data points within $z \sim 0.5$ to 2.0 (shown in filled triangles) and those at $z < 1.0$ (shown in filled diamonds) are from Connolly et al. (1997) and Lilly et al. (1996), respectively. These were adjusted to $\Omega_{\rm M} = 0.3$, $\Omega_\Lambda = 0.7$ cosmology and to represent the star-formation density estimated by UV luminosities from objects with $M_{\rm UV} - 5 \log h \leq -20$. The conversion factors from the UV luminosity (at rest-frame 1500Å for $z \sim 3$ to 5 and 2800Å for $z < 2$) to the star-formation density are from Madau et al. (1998). The filled symbols indicate the values without any correction for dust extinction. Dust extinction was corrected following the prescription by Calzetti et al. (2000) with $E(B-V) = 0.15$ for all data points. The values are shown by the open symbols. The assumed cosmology is $\Omega_{\rm M} = 0.3$, $\Omega_\Lambda = 0.7$.

from $z = 0$ to 2, and appears to be almost constant, or slowly declining, at a larger redshift. This tendency has been reproduced by recent hydrodynamical simulations (e.g., Nagamine et al. 2001; Ascasibar et al. 2002) and semi-analytic models of galaxy formation, which take collisional starburst into account (Somerville et al. 2001; Balland et al. 2002). It is hard to make a direct comparison of the observed data and these predictions, because the observations (especially for high-redshift objects) are restricted to trace only the bright part of the luminosity function. Although it would be desirable for model predictions with an integration range comparable to the observational limit to be available, we do not know such predictions among the recently published semi-analytic models and numerical simulations; they usually give the total star-formation density. The shape of the faint end of the luminosity function has a crucial effect on the UV luminosity density, and may differ depending on the redshift. It is also needed to consider the uncertainty of dust extinction in the UV luminosity; the correction factor often amounts to more than 3. We might be able to say, however, that if we assume that the shape of the UV luminosity function and the degree of dust extinction do not change significantly with respect to the redshift, recent semi-analytic models with collisional starburst such as by Somerville et al. (2001), and hydrodynamical simulations such as by Ascasibar et al. (2002), are broadly consistent with the observed data, including our result for $z \sim 5$.

5.3. Contribution of Stellar Sources to the Ionizing Photon Density in the Intergalactic Medium

Finally, we briefly comment on the contribution of stellar sources to the hydrogen-ionizing radiation field at $z \sim 5$. Recently, Steidel et al. (2001) claimed that the escape fraction $f_{\rm esc}$, which represents the rate of Lyman continuum photons emitted outside from a galaxy, of the LBGs at $z \sim 3$ is significantly higher than the observational upper limit for star-forming galaxies in the local universe; it is comparable toi, or larger than, 0.5 [but Giallongo et al. (2002) made a deep spectroscopic observation for two LBGs and placed upper limit of $f_{\rm esc} < 0.16$]. Steidel et al. (2001) estimated the contribution of LBGs at $z \sim 3$ to the ionizing radiation field at 1 ryd to be $(1.2 \pm 0.3) \times 10^{26} h$ erg s^{-1} Hz^{-1} Mpc^{-3}, which is about 5-times larger than the contribution from quasars at the same redshift (Madau et al. 1999). If the rapid decrease of the quasar number density at $z > 3$ (Fan et al. 2001 and references therein) is real, the number of ionizing photons radiated from quasars should strongly declines at higher redshifts. Madau et al. (1999) estimated that it drops by a factor of $\sim$2 from $z = 3$ to $z = 5$. Provided that the escape fraction of LBGs at $z \sim 5$ is as large as 0.5, our estimate of the UV luminosity density at $z \sim 5$ implies that the ionizing photons originated from star-forming galaxies are $\sim$5 to 7-times larger than those from quasars at the same redshift. This further suggests that the source of the UV photons that reionized the Universe sometime at $z > 5$ is dominated by stellar origin. It is also interesting that the combination of the estimated numbers of the ionizing photons from LBGs and quasars at $z \sim 5$ is comparable to the number of photons needed to fully ionize the universe considered in Madau et al. (1999) (Einstein–de Sitter universe with a clumping factor of 30 and a baryon fraction of $\Omega_b h^2 = 0.02$). However, this coincidence is based on quite uncertain factors, such as the quasar number density, the escape fraction of ionizing photons, and the clumpiness of the hydrogen gas in the early universe. A deep observation of the rest-frame far-UV wavelengths of LBGs is one of the indispensable subjects needed to clarify the nature of the ionizing radiation field at $z > 3$.

6. Summary and Conclusion

We have presented the results of a search for Lyman break galaxies at a redshift range between 4.4 and 5.3 in the field including the HDF-North with Suprime-Cam attached to the Subaru telescope. Databases for galaxies in the HDF-N and its flanking fields enable us to find the best color selection criteria with least foreground contamination. Within the surveyed area of 618.6 arcmin^2, we have found 96 LBG candidates with $23.0 < I_c \leq 24.5$ mag, and 310 candidates with $I_c \leq 25.5$ mag. There is a hint of a deficiency of bright blue galaxies, although it is not as clear as suggested for LBGs at $z \sim 3$ to 4.

The contamination of objects at intermediate redshifts was estimated by employing a resampling algorithm. The fraction of contamination amounts to $\sim$20% at the bright part

of the sample, and ∼50% at the faintest magnitude range. We also performed Monte Carlo simulations to evaluate the incompleteness of the survey. The completeness was estimated as a function of the magnitude and the redshift of an object; in the redshift range of $4.5 \lesssim z \lesssim 5.0$, it is ∼80% in the bright part of the sample and ∼20% in the faintest magnitude range. Using these corrections, we derived the luminosity function of LBGs at $z \sim 5$ statistically in the absolute UV magnitude range from −23.0 to −20.5 (with $\Omega_{\rm M} = 0.3$, $\Omega_\Lambda = 0.7$, $h_0 = 0.65$). No significant difference was found between the luminosity function of LBGs at $z \sim 5$ and those at $z \sim 3$ and 4 obtained by Steidel et al. (1999), though there might be a decrease in the number density at a fainter magnitude. We compared the UV luminosity density at a redshift of 5 to those at $z \sim 3$ and 4. If we adopt a direct sum of the luminosity function within our observational limit, the star-formation density decreases to 56–69% of that at $z \sim 3$, estimated by Steidel et al. (1999). This decrease in the UV luminosity density at $z \sim 5$, compared to $z \sim 3$, is due to the smaller number density of faint galaxies at $z \sim 5$. We cannot rule out the possibility that the UV luminosity density is almost constant at $z \gtrsim 3$, if we take into account the larger uncertainty in the faint part of the luminosity function.

We have discussed a plausible evolutionary scenario of LBGs based on our results. The similarity of the luminosity functions at redshifts of 5 to 3 implies that most of the LBGs at $z \sim 5$ should have faded out at $z \sim 3$ and that the LBGs at $z \sim 5$ are different galaxies from those seen at $z \sim 3$, if we take the face values for the ages of the LBGs at $z \sim 3$ obtained by the SED fitting in which a continuous star formation in an individual galaxy is assumed. However, if the star formation in LBGs is sporadic, the similarity of the luminosity function at $z \sim 3$ and 5 would be naturally explained. Such sporadic star formation has been suggested by hydrodynamical simulations and semi-analytic models with collisional starbursts; the trend of the cosmic star-formation history predicted by these studies resembles that estimated from integrating the UV luminosity density within the observational limit.

We thank all of the staff members of the Subaru telescope during our observations, especially Yutaka Komiyama, for their devoted support and technical assistance. We also appreciate the Suprime-Cam group members, especially Masami Ouchi, for their kind advice and discussions concerning data-reduction procedures. We also thank the referees for the comments which improved the paper. I.I. is supported by a Research Fellowship of the Japan Society for the Promotion of Science for Young Scientists.

References

Adelberger, K. L., & Steidel, C. C. 2000, ApJ, 544, 218

Ascasibar, Y., Yepes, G., Gottlöber, S., & Müller, V. 2002, A&A, 387, 396

Balland, C., Devriendt J. E. G., & Silk J. 2002, preprint (astro-ph/0210030)

Barger, A. J., Cowie, L. L., Brandt, W. N., Capak, P., Garmire, G. P., Hornschemeier, A. E., Steffen,

A. T., & Wehner, E. H. 2002, AJ, 124, 1839
Baugh, C. M., Cole, S., Frenk, C. S., & Lacey, C. G. 1998, ApJ, 498, 504
Becker, R. H., et al. 2001, AJ, 122, 2850
Bertin, E., & Arnouts, S. 1996, A&AS, 117, 393
Calzetti, D., Armus, L., Bohlin, R. C., Kinney, A. L., Koornneef, J., & Storchi-Bergmann, T. 2000, ApJ, 533, 682
Casertano, S., et al. 2000, AJ, 120, 2747
Castelli F., & Kurucz R. L. 1994, A&A, 281, 817
Cohen, J. G., Hogg, D. W., Blandford, R., Cowie, L. L., Hu, E., Songaila, A., Shopbell, P., & Richberg, K. 2000, ApJ, 538, 29
Coleman, G. D., Wu, Chi-Chao, & Weedman, D. W. 1980, ApJS, 43, 393
Connolly, A. J., Szalay, A. S., Dickinson, M., Subbarao, M. U., & Brunner, R. J. 1997, ApJ, 486, L11
Dawson, S., Spinrad, H., Stern, D., Dey, A., Breugel, W. V., De Vries, W., & Reuland, M. 2002, ApJ, 570, 92
Dawson, S., Stern, D., Bunker, A. J., Spinrad, H., & Dey, A. 2001, AJ, 122, 598
Dey, A., Spinrad, H., Stern, D., Graham, J. R., & Chaffee, F. H. 1998, ApJ, 498, L93
Ellis, R., Santos, M. R., Kneib, J-P, Kuijken, K. 2001, ApJ, 560, L119
Fan, X., et al. 2001, AJ, 121, 54
Ferguson, H. C., Dickinson, M., & Papovich, C. 2002, ApJ, 569, L65
Fernández-Soto, A., Lanzetta, K. M., & Yahil, A. 1999, ApJ, 513, 34
Giallongo, E., Cristiani, S., D'Odorico, S., & Fontana, A. 2002, ApJ, 568, L9
Giavalisco, M., Steidel, C. C., Adelberger, K. L., Dickinson, M. E., Pettini M., & Kellogg, M. 1998, ApJ, 503, 543
Giavalisco, M. & Dickinson, M. 2001, ApJ, 550, 177
Irwin M., Maddox S., & McMahon R. 1994, Spectrum, 2, 14
Kodama, T., & Arimoto, N. 1997, A&A, 320, 41
Landolt, A.U. 1992, AJ, 104, 340
Lilly, S. J., Le Fevre, O., Hammer, F., & Crampton, D. 1996, ApJ, 460, L1
Madau, P. 1995, ApJ, 441, 18
Madau, P., Ferguson, H. C., Dickinson, M. E., Giavalisco, M., Steidel, C. C., & Fruchter, A. 1996, MNRAS, 283, 1388
Madau, P., Haardt, F., & Rees, M. J. 1999, ApJ, 514, 648
Madau, P., Pozzetti, L., & Dickinson, M. 1998, ApJ, 498, 106
Meurer, G. R., Heckman, T. M., & Calzetti, D. 1999, ApJ, 521, 64
Miyazaki, S., et al. 2002, PASJ, 54, 833
Monet, D., et al. 1998, The USNO-A2.0 Catalogue, (U.S. Naval Observatory, Washington DC).
Nagamine, K. 2002, ApJ, 564, 73
Nagamine, K., Fukugita, M., Cen, R., & Ostriker, J. P. 2001, ApJ, 558, 497
Ouchi, M., et al. 2001a, ApJ, 558, L83
Ouchi, M., et al. 2001b, in The Proceedings of the Marseille 2001 Conference "Where is the

Matter? Tracing Dark and Bright Matter with the New Generation of Large-Scale Surveys" (astro-ph/0109252)

Papovich, C., Dickinson, M., & Ferguson, H. C. 2001, ApJ, 559, 620

Pettini, M., Shapley, A. E., Steidel, C. C., Cuby, J.-G., Dickinson, M., Moorwood, A. F. M., Adelberger, K. L., & Giavalisco, M. 2001, ApJ, 554, 981

Pickles, A.J. 1998, PASP, 110, 863

Sawicki, M. & Yee, H. K. C. 1998, AJ, 115, 1329

Shapley, A. E., Steidel, C. C., Adelberger, K. L., Dickinson, M., Giavalisco, M., & Pettini, M. 2001, ApJ, 562, 95

Somerville, R. S., Primack, J. R., & Faber, S. M. 2001, MNRAS, 320, 504

Spinrad, H., Stern, D., Bunker, A., Dey, A., Lanzetta, K., Yahil, A., Pascarelle, S., & Fernández-Soto, A. 1998, AJ, 116, 2617

Steidel, C. C., Adelberger, K. L., Dickinson, M., Giavalisco, M., Pettini, M., & Kellogg, M. 1998, ApJ, 492, 428

Steidel, C. C., Adelberger, K. L., Giavalisco, M., Dickinson, M., & Pettini, M. 1999, ApJ, 519, 1

Steidel, C. C., Giavalisco, M., Dickinson, M., & Adelberger, K. L. 1996a, AJ, 112, 352

Steidel, C. C., Giavalisco, M., Pettini, M., Dickinson, M., & Adelberger, K. L. 1996b, ApJ, 462, L17

Steidel, C. C., & Hamilton, D. 1992, AJ, 104, 941

Steidel, C. C., Pettini, M., & Adelberger, K. L. 2001, ApJ, 546, 665

Stern, D., & Spinrad, H. 1999, PASP, 111, 1475

Teplitz, H. I., et al. 2000, ApJ, 542, 18

Tresse L., Maddox S. J., Le Fèvre O., & Cuby J.-G. 2002, MNRAS, 337, 369

Tyson, J. A. 1988, AJ, 96, 1

Weymann, R. J., Stern, D., Bunker, A., Spinrad, H., Chaffee, F. H., Thompson, R. I., & Storrie-Lombardi, L. J. 1998, ApJ, 505, L95

Williams, R. E., et al. 1996, AJ, 112, 1335